



**HAL**  
open science

# Combined physical and biogeochemical assessment of mesoscale eddy parameterisations in ocean models: eddy-induced advection at eddy-permitting resolutions

Xi Ruan, Damien Couespel, Marina Lévy, J. Li, J. Mak, Y. Wang

## ► To cite this version:

Xi Ruan, Damien Couespel, Marina Lévy, J. Li, J. Mak, et al.. Combined physical and biogeochemical assessment of mesoscale eddy parameterisations in ocean models: eddy-induced advection at eddy-permitting resolutions. 2024. hal-04605065

**HAL Id: hal-04605065**

**<https://cnrs.hal.science/hal-04605065v1>**

Preprint submitted on 7 Jun 2024

**HAL** is a multi-disciplinary open access archive for the deposit and dissemination of scientific research documents, whether they are published or not. The documents may come from teaching and research institutions in France or abroad, or from public or private research centers.

L'archive ouverte pluridisciplinaire **HAL**, est destinée au dépôt et à la diffusion de documents scientifiques de niveau recherche, publiés ou non, émanant des établissements d'enseignement et de recherche français ou étrangers, des laboratoires publics ou privés.

# Combined physical and biogeochemical assessment of mesoscale eddy parameterisations in ocean models: eddy-induced advection at eddy-permitting resolutions

X. Ruan<sup>a,1</sup>, D. Couespel<sup>b,c</sup>, M. Lévy<sup>c</sup>, J. Li<sup>a,d</sup>, J. Mak<sup>a,e,1</sup>, Y. Wang<sup>a,d</sup>

<sup>a</sup>Department of Ocean Science, Hong Kong University of Science and Technology

<sup>b</sup>NORCE Norwegian Research Centre, Bjerknes Centre for Climate Research

<sup>c</sup>Sorbonne Université, LOCEAN-IPSL, CNRS/IRD/MNHN

<sup>d</sup>Center for Ocean Research in Hong Kong and Macau, Hong Kong University of Science and Technology

<sup>e</sup>National Centre of Oceanography, Southampton

---

## Abstract

Ocean general circulation models at the eddy-permitting regime are known to under-resolve the mesoscale eddy activity and associated eddy-mean interaction. Under-resolving the mesoscale eddy field has consequences for the resulting mean state, affecting the modelled ocean circulation and biogeochemical responses, and impacting the quality of climate projections. There is an ongoing debate on whether and how a parameterisation should be utilised in the eddy-permitting regime. Focusing on the Gent–McWilliams (GM) based parameterisations, it is known that, on the one hand, not utilising a parameterisation leads to insufficient eddy feedback and results in biases. On the other hand, utilising a parameterisation leads to double-counting of the eddy feedback, and introduces other biases. A recently proposed approach, known as *splitting*, modifies the way GM-based schemes are applied in eddy-permitting regimes, and has been demonstrated to be effective in an idealised Southern Ocean channel model. In this work, we evaluate whether the splitting approach can lead to improvements in the physical and biogeochemical responses in an idealised double gyre model. Compared with a high resolution mesoscale eddy resolving model truth, the use of the GM-based GEOMETRIC parameterisation together with splitting in the eddy-permitting regime leads to broad improvements in the control pre-industrial scenario and an idealised climate change scenario, over models with and models without the GM-based GEOMETRIC parameterisation active. While there are still some deficiencies, particularly in the subtropical region where the transport is too weak and may need momentum re-injection to reduce the biases, the present work provides further evidence in support of using the splitting procedure together with a GM-based parameterisation in ocean general circulation models at eddy-permitting resolutions.

**Keywords:** scale-aware mesoscale eddy parameterisation, ocean circulation, climate change, numerical modelling, biophysical interactions

---

## 1. Introduction

Mesoscale eddy effects are essential for shaping the ocean circulation, marine ecosystems and global climate via the associated eddy-mean interaction (e.g., Griffies et al., 2015; Fox-Kemper et al., 2019; Beech et al., 2022). One such effect is the slumping of isopycnals that is normally associated with baroclinic instability, which releases the large-scale available potential energy (from input via Ekman processes, buoyancy forcing or otherwise) into small-scale eddy energy (e.g, Gent and McWilliams, 1990; Gent et al., 1995), with associated impacts on the mean stratification. Another is the additional diffusion of tracers, such as thermodynamic or biogeochemical variables, along isoneutral directions (e.g., Redi, 1982; Griffies, 1998; Jones and Abernathy, 2019; Holmes et al., 2022), which can affect the

---

Email addresses: xruanaa@connect.ust.hk (X. Ruan), julian.c.l.mak@gmail.com (J. Mak)

<sup>1</sup>Corresponding authors.

9 ventilation rate of tracers (although there are recent works that suggest such isoneutral diffusion can also have a  
10 non-negligible effect on shaping the stratification; e.g., Chouksey et al. 2022). Yet another is the re-injection of eddy  
11 energy back into larger-scales and forcing the larger-scale circulation (e.g., Charney, 1971; Waterman and Jayne, 2012;  
12 Waterman and Hoskins, 2013; Bachman, 2019). The representation of such processes in numerical ocean models can  
13 have a leading order impact on the resulting model responses (e.g., Fox-Kemper et al., 2019). Thus, it is important  
14 to quantify the impacts of such eddy effects on the model responses, which constrains future model projections and  
15 their dependence on eddy processes, and helps inform management and policy decisions (e.g., Hoegh-Guldberg et al.,  
16 2014; Hewitt et al., 2020).

17 Most ocean models employed thus far for Earth System Models are *coarse resolution models*, in which the models  
18 do not permit an explicit representation of ocean mesoscale eddy effects. Eddy effects are often parameterised in these  
19 models, such as by the Gent–McWilliams (GM) based schemes to mimic the slumping of isopycnals (e.g., Gent and  
20 McWilliams, 1990; Gent et al., 1995; Eden and Greatbatch, 2008; Marshall et al., 2012; Mak et al., 2022b), diffusion  
21 of tracers along the isoneutral direction (e.g., Redi, 1982; Griffies, 1998; Holmes et al., 2022), momentum backscatter  
22 to re-inject eddy energy (e.g., Bachman, 2019; Jansen et al., 2019; Juricke et al., 2020; Yankovsky et al., 2023), or  
23 possibly related machine learning approaches (e.g., Perezhogin et al., 2023). While many works consider the physical  
24 or biogeochemical response to such parameterisations (e.g., Pradal and Gnanadesikan, 2014; Berthet et al., 2019;  
25 Swearer et al., 2019; Séférian et al., 2019; Mak et al., 2022b), of particular relevance to the present work are those  
26 of Couespel et al. (2021) and Ruan et al. (2023), who consider the *joint* physical and biogeochemical response to  
27 parameterisation choices. Those works, although within the context of idealised ocean models and simplified climate  
28 change scenarios, comprehensively assess both responses in coarse resolution models, highlighting how some choices  
29 of GM-based parameterisations are able to improve aspects of the model responses and sensitivities. In particular,  
30 the work of Ruan et al. (2023) highlights a case where one can obtain a reasonable biogeochemical response but for  
31 an essentially inconsistent physical response, i.e., where we get a ‘right’ response but not necessarily for the ‘right’  
32 reasons.

33 The present work builds upon the previous work of Ruan et al. (2023) in coarse resolution models, by performing  
34 an analogous examination in the *eddy-permitting* regime. With increasing computational power, it is increasingly  
35 feasible to allow for an explicit representation of mesoscale eddies in numerical ocean models, even in global  
36 configuration Earth System Models. While it is known that increasing the spatial resolution of the ocean models  
37 can lead to a reduction of model biases (e.g., Roberts et al., 2020; Hewitt et al., 2020, 2022; Beech et al., 2022),  
38 other issues arise, particularly as to whether mesoscale eddy parameterisations should be dispensed with or employed,  
39 and if employed, how they are employed. Without parameterisations, it is known that the eddy processes are mis-  
40 represented, and the associated eddy-mean feedback is too weak. On the other hand, it is known that GM-based  
41 parameterisations utilised as-is end up damping explicit eddy fluctuations. One suggestion then is to switch off the  
42 GM-based parameterisations when the model is regarded as eddy-permitting, via the use of a resolution function (e.g.,  
43 Hallberg, 2013). Another is to accept there is some damping by GM-based schemes, but re-energise via backscatter  
44 approaches (e.g., Jansen et al., 2015b,a, 2019; Bachman, 2019). A proposal considers anisotropic versions of the GM-  
45 based parameterisation (e.g., Smith and Gent, 2004). Some works advocate for backscatter *only* (e.g., Juricke et al.,  
46 2020; Chang et al., 2023; Yankovsky et al., 2023), arguing that backscatter re-energises the explicit eddy activity and  
47 catalyses for the extra eddy-mean interaction, although whether this is in fact true is to be convincingly demonstrated.

48 In the present work, the principal focus is on quantifying the benefits and/or deficiencies arising from a procedure  
49 suggested by Mak et al. (2023) termed field *splitting*, which modifies the way GM-based schemes are applied.  
50 No resolution function, anisotropic GM, backscatter isoneutral diffusion is employed in this work, although the  
51 splitting procedure is not necessarily mutually exclusive of those modelling choices. We apply the splitting procedure  
52 to the model and experimental procedure of Ruan et al. (2023) in the eddy-permitting regime, where we expect  
53 improvements for reasons to be detailed. The present work further tests the splitting procedure for a model in  
54 a different ocean-relevant setting (a representative mid-latitude gyre system), and comprehensively assesses both  
55 the modelled physical and biogeochemical responses, to inform future works using more realistic physical settings,  
56 biogeochemical models, and/or forcing scenarios of more direct relevance to climate projection exercises.

57 In §2, we provide the technical problem statement relating to the use of a GM-based parameterisation in an  
58 eddy-permitting regime, as well as the motivation and overview for the splitting procedure of Mak et al. (2023). We  
59 leverage the model and experimental procedure based largely on the previous work of Ruan et al. (2023) to test our  
60 scientific hypotheses, but with the caveat that the results we present in the main body of the work do not employ

any isoneutral diffusion, for reasons to be elaborated upon. In §3 we provide a detailed comparison of the physical and biogeochemical responses in the set of models under a control pre-industrial scenario. In §4 we consider the analogous responses under an idealised climate change scenario, and additionally assess the associated sensitivities. The paper closes with conclusions and discussions in §5, detailing implications, limitations and outlooks in light of the present results. In Appendix A, we reiterate and further elaborate on why the present work does not include isoneutral diffusion, and provide sample numerical evidence on why there are subtleties with the use of isoneutral diffusion together with *state-aware* GM-based parameterisations, such as that employed in this work.

## 2. Problem statement, field splitting approach, and numerical set up

### 2.1. Problem statement

The underlying problem in this work relates to whether and how a GM-based parameterisation should be used when the model allows for an explicit representation of mesoscale eddies. Consider a Reynolds decomposition of the velocity (specifically, the advective velocity in the tracer equation only)

$$\mathbf{u} = \overline{\mathbf{u}} + \mathbf{u}' + \mathbf{u}^*, \quad \overline{\mathbf{u}'} = 0, \quad (1)$$

where an overbar denotes a Reynolds average (time-average is considered in this work), a prime denotes a deviation from that average such that the average of the deviation is zero (so  $\mathbf{u}'$  is associated with the *explicit* eddies), and a star denotes any parameterised component we may wish to add on (so  $\mathbf{u}^*$  is associated with the *parameterised* eddies). In the eddy-rich/resolving case without a parameterisation, we would set  $\mathbf{u}^* = 0$ . In a coarse resolution calculation,  $\mathbf{u}'$  would be effectively zero, and we might mimic the effect of the missing  $\mathbf{u}'$  by  $\mathbf{u}^*$ , such as via the GM specification (e.g., Gent et al., 1995)

$$\mathbf{u}^* = \nabla \times (\mathbf{e}_z \times \kappa_{\text{gm}} \mathbf{s}), \quad \mathbf{s} = \frac{\nabla_H \rho}{-\partial \rho / \partial z}, \quad (2)$$

where  $\nabla$  is the gradient operator ( $\nabla_H$  is the gradient operator only in the horizontal),  $\mathbf{e}_z$  is the unit vector pointing in the vertical,  $\kappa_{\text{gm}}$  is the GM or eddy-induced velocity coefficient (in units of  $\text{m}^2 \text{s}^{-1}$ ),  $\mathbf{s}$  is the vector encoding the isopycnal slopes in the horizontal directions, and  $\rho$  denotes the relevant density variable of interest.

A modelling problem in the eddy-permitting regime is that  $\mathbf{u}'$ , while weak, is not necessarily negligible, and the question is whether  $\mathbf{u}^*$  should be included or not. If  $\mathbf{u}^* = 0$  (by setting  $\kappa_{\text{gm}} = 0$  for example), then the explicit eddies are too weak, leading to a rather weak feedback onto the mean state. As such, we might expect the resulting baroclinic mean flow to be too strong, associated for example with an overly deep stratification (e.g., Fig. 7c of Mak et al., 2023), resulting in an overly strong meridional overturning circulation. A larger lateral transport in the present double-gyre system to be investigated would be expected to lead to meridional heat transport with positive biases, while the larger vertical transport might be expected to lead to larger Net Primary Production (NPP) via increased nutrient upwelling.

One might suspect some degree of  $\mathbf{u}^*$  would need to be included. However, that presents another set of problems, in that  $\mathbf{u}^*$  from the GM-based parameterisations tends to dominate and damps the explicit  $\mathbf{u}'$  that would be permitted by the model at the relevant spatial resolution. The result is often an eddy-permitting resolution calculation that strongly resembles a coarse resolution model (e.g., Fig 2c of Mak et al., 2023), but at a higher computational cost. The physical rationalisation of this effect is summarised in Fig. 3a of Mak et al. (2023): in the eddy-permitting regime, explicit eddies are still in the geostrophic regime, so velocity fluctuations are associated with isopycnal fluctuations via the thermal wind shear relation. Since GM-based schemes act to mimic baroclinic instability by flattening isopycnals, the isopycnal fluctuations associated with explicit eddies are rapidly damped by the GM-based schemes. As a result, we would expect the performance of the double-gyre model to largely mimic that of the coarse resolution model, with an overturning circulation that is too weak, with positive biases in heat transport, nutrient transport and associated NPP (cf. coarse resolution simulations in Ruan et al., 2023).

To combat the overly diffuse nature of the model in the eddy-permitting regime (without or with GM-based schemes active), approaches based on momentum backscatter have been proposed (e.g., Bachman, 2019; Jansen et al., 2019; Juricke et al., 2020), with the idea that backscatter would strengthen the explicit eddies and catalyse for the extra eddy-mean feedbacks (e.g., Chang et al., 2023; Yankovsky et al., 2023). While there are model improvements as a result of employing only backscatter, it remains to be convincingly demonstrated that backscatter approaches really are supplementing for the extra eddy-mean interaction in the intended fashion.

## 106 2.2. A field splitting approach for eddy-permitting calculations

107 The recent work of Mak et al. (2023) revisits the issue of the co-existence of  $\mathbf{u}'$  and  $\mathbf{u}^*$ , and argues that  $\mathbf{u}^*$  from a  
 108 GM-based scheme arises from the collective action of eddies with some sufficiently large-scale region, acting over that  
 109 same region that should be regarded as eddy-free after the averaging procedure. Since the use of a GM-based scheme  
 110 as-is in an eddy-permitting model where the state explicitly represents eddies violates the initial working assumption,  
 111 it is perhaps not surprising that the GM-based schemes have associated modelling deficiencies in the eddy-permitting  
 112 regime. If one accepts that argument, then a relatively simple fix would be a field *splitting* approach. Consider a  
 113 decomposition of the density field as

$$\rho = \rho_L + \rho_S, \quad (3)$$

114 where  $\rho_L$  is some large-scale density field associated with some non-eddy field, and  $\rho_S$  is the residual between  
 115 the full and large-scale density field. We simply use  $\rho_L$  as the input field for the parameterisation (i.e., let  $\rho \rightarrow \rho_L$   
 116 and  $s \rightarrow s_L$  in Eq. 2, which gives  $\mathbf{u}_L^* = \nabla \times (\mathbf{e}_z \times \kappa_{\text{gm}} s_L)$ , and proceed as usual. The observation is that  $\mathbf{u}_L^*$  is now  
 117 fundamentally a large-scale object at a smaller magnitude, because the input field is large-scale, and the gradient of  
 118 a quantity that is smooth on the large-scale is of smaller magnitude at the grid-scale. Such an approach should in  
 119 principle allow  $\mathbf{u}'$  and  $\mathbf{u}_L^*$  to co-exist (see the schematic given in Fig. 3b of Mak et al., 2023).

120 The work of Mak et al. (2023) reports that, in an idealised Southern Ocean configuration, the mean-state  
 121 improvements appear to require the use of the splitting procedure, and the improvements cannot be attained by  
 122 switching off the parameterisation or by tuning the parameterisation in the absence of splitting (cf. Fig. 7 Mak et al.,  
 123 2023). In the double-gyre model at the eddy-permitting resolution to be detailed, relative to the model without a GM-  
 124 based parameterisation, we would expect that the use of splitting together with a GM-based parameterisation reduces  
 125 the overly deep stratification, the overly strong meridional overturning circulation, and the overly large NPP resulting  
 126 from the larger nutrient transport. Further, we hypothesise that the use of splitting would lead to improvements that  
 127 cannot be achieved by a model with a GM-based parameterisation without splitting via tuning the free parameters.

## 128 2.3. Model set up

129 To test for the aforementioned hypotheses and quantify the benefits and/or deficiencies afforded to the modelled  
 130 physical and biogeochemical responses by the splitting procedure, we employ a double-gyre model coupled to an  
 131 idealised biogeochemistry model LOBSTER (cf. Lévy et al., 2010, 2012); the model is essentially that reported in  
 132 Couespel et al. (2021) and Ruan et al. (2023), and here we only recap the essentials (see Ruan et al., 2023, for in-  
 133 depth details). The model is created in the Nucleus for European Modelling of the Ocean framework (NEMO, version  
 134 4.0.5 r14538; Madec 2008). The domain of the double-gyre model is a ‘straightened’ version of the NEMO rotated  
 135 gyre configuration test case. The square domain has sides of length  $L = 3180$  km, employing a regular horizontal  
 136 grid-spacing. The model is on a  $\beta$ -plane centred at around  $35^\circ$  N, extending to  $20^\circ$  N to the south and  $50^\circ$  N to the  
 137 north. The lateral boundary momentum condition of each side is set to be free slip, and a non-linear drag is applied  
 138 on the bottom boundary.

139 Given that the bathymetry can have impacts on the large-scale circulation and thus affect the physical and  
 140 biogeochemical representations, we consider a model with a slope on the west and east sides in this study, in contrast  
 141 to the previous works of Couespel et al. (2021) and Ruan et al. (2023) with no bathymetry. Following the work of  
 142 Jackson et al. (2006), we consider a bottom bathymetry that varies only in the zonal direction, given by (in units of m)

$$H = 100 + (H_i - 100) \left[ 1 - e^{-x^2/\sigma^2} - e^{-(L-x)^2/\sigma^2} \right], \quad (4)$$

143 where  $H_i = 4$  km is the total depth of the modelled ocean (the ocean is shallowest at 100 m),  $x$  is the offshore distance  
 144 from the western boundary,  $L$  is the width of the domain, and  $\sigma$  is taken to be 100 km (roughly corresponding to the  
 145 choice of  $1^\circ$  employed in Jackson et al. 2006). In the NEMO model, 31 uneven vertical layers are employed, in line  
 146 with the standard gyre test case, and the vertical coordinate is chosen to be in  $z$ -coordinate with partial steps. The main  
 147 consequence of employing such a bathymetry is a slight southward shift of the modelled Western Boundary Current  
 148 relative to the relevant previous works with no bathymetry (Couespel et al., 2021; Ruan et al., 2023). The qualitative  
 149 conclusions we draw from this work are robust and carry over to the case with no bathymetry (not shown).

150 The key model parameter settings of the set of calculations are displayed in Table 1. Tracer and momentum  
 151 lateral diffusion are in the *geopotential* direction for all models reported here. Tracer advection is still with the

|   | 1/4° (R4, SPLIT and GEOM)   | 1/12° (R12)   |
|---|---|---|
| Horizontal resolution $\Delta x = \Delta y$ | 26.5 km   | 8.83 km   |
| Time step $\Delta t$                        | 20 mins   | 10 mins   |
| Tracer diffusion $\kappa_T$                 | Geopotential bi-Laplacian $\nabla^4$ , $-5 \times 10^9 \text{ m s}^{-4}$      | Geopotential bi-Laplacian $\nabla^4$ , $-10^9 \text{ m s}^{-4}$             |
| Momentum diffusion $\kappa_M$               | Geopotential bi-Laplacian $\nabla^4$ , $-2.5 \times 10^{11} \text{ m s}^{-4}$ | Geopotential bi-Laplacian $\nabla^4$ , $-3 \times 10^{10} \text{ m s}^{-4}$ |
| Tracer advection                            | MUSCL   | MUSCL   |
| Momentum advection                          | Centered standard kinetic energy scheme                                       | Centered standard kinetic energy scheme                                     |

|                                       | SPLIT                            | GEOM                             |
|---------------------------------------|----------------------------------|----------------------------------|
| Tuning parameter $\alpha$             | 0.065                            | 0.065                            |
| Energy diffusivity $\eta_E$           | $500 \text{ m}^2 \text{ s}^{-1}$ | $500 \text{ m}^2 \text{ s}^{-1}$ |
| Minimum energy level $E_0$            | $1.0 \text{ m}^3 \text{ s}^{-2}$ | $1.0 \text{ m}^3 \text{ s}^{-2}$ |
| Dissipation time-scale $\lambda^{-1}$ | 135 days                         | 135 days                         |
| Filter length scale $L$               | 100 km                           | —                                |
| Pre-conditioning param. $\gamma$      | 75                               | —                                |

Table 1: Key model parameter values of the set of calculations.

MUSCL scheme. Momentum advection is processed in vector form with a second order centered scheme, and the vertical mixing is parameterised by the turbulent kinetic energy closure of Gaspar et al. (1990). We keep the choice of linear equation of state, so that the splitting approach as implemented in Mak et al. (2023) using a filtered temperature and salinity field to compute the resulting large-scale density field  $\rho_L$  can be used without further modifications. The zonally symmetric atmospheric forcing employs the flux formulation, with a predetermined repeating seasonal cycle for the wind stress, penetrative solar radiation, pseudo-atmospheric temperature and freshwater flux. For more details, see Fig. 1 of Lévy et al. (2010) or Ruan et al. (2023).

To reiterate, no isoneutral diffusion is employed in the results provided in the main body of the present article. While this might be counter to standard practices, the reason is that there appears to be a positive feedback loop when isoneutral diffusion is utilised with *state-aware* GM-based parameterisations, leading to further changes in the stratification, affecting the various physical and biogeochemical responses. The positive feedback loop is elaborated upon in Appendix A, where we also provide supporting numerical evidence for such a positive feedback loop, but also isoneutral diffusion can lead to non-negligible damping of the explicit variability in the eddy-permitting regime. Both effects lead to non-trivial model responses, and we focus only on the GM-based parameterisation in the present article for simplicity.

The model employs the simplified biogeochemistry model LOBSTER, which takes nitrogen as the currency, solving six biogeochemical variables of phytoplankton, zooplankton, detritus, dissolved organic matter, nitrate and ammonium (e.g., Lévy et al., 2012). The uptake of nitrate and ammonium by phytoplankton determined as the Net Primary Production (NPP) is of particular interest in this study. The absence of physiological changes represented in the idealised model means the plankton is primarily affected by the modelled flow and the related advective tendencies, and a dominant control on NPP is the nutrient supply over the large length-scales via the modelled circulation.

For the present work, the GM-based parameterisation that we primarily focus on is the GM-version of the GEOMETRIC (Marshall et al., 2012; Mak et al., 2018, 2022b), given its use in the previous work of Ruan et al. (2023) for the coarse resolution case, and other works that have demonstrated the use of GEOMETRIC leads to various improvements in the modelled mean state (Mak et al., 2018, 2022b, 2023; Wei et al., 2024). Via the analysis given in Mak et al. (2023), if the splitting approach (given essentially by Eq. (2) with  $\rho \rightarrow \rho_L$  and  $s \rightarrow s_L$ ) is to be used with GEOMETRIC, for consistency we should take

$$\kappa_{\text{gm}} = \alpha \frac{\int E \, dz}{\int (M_L^2 / N_L) \, dz}, \quad (5)$$

where  $\alpha$  is a non-dimensional tuning parameter ( $|\alpha| \leq 1$ ),  $E$  is the total (potential and kinetic) parameterised eddy energy,  $M_L^2 \sim |\nabla_H \rho_L|$  is the large-scale horizontal buoyancy frequency, and  $N_L^2 \sim -\partial \rho_L / \partial z$  is the large-scale vertical buoyancy frequency. The vertical integration in Eq. 5 results in a time and horizontally varying  $\kappa_{\text{gm}}(x, y, t)$ , and the

182 depth-integrated total parameterised eddy energy is prognostically constrained by the eddy energy budget

$$\frac{d}{dt} \int E \, dz + \underbrace{\nabla_H \cdot \left( \bar{\mathbf{u}}^z - |c| \mathbf{e}_x \right) \int E \, dz}_{\text{advection}} = \underbrace{\int \kappa_{\text{gm}} \frac{M_L^4}{N_L^2} \, dz}_{\text{source}} - \underbrace{\lambda \int (E - E_0) \, dz}_{\text{dissipation}} + \underbrace{\eta_E \nabla_H^2 \int E \, dz}_{\text{diffusion}}. \quad (6)$$

183 Here, the source of eddy energy with the use of a splitting approach stems from large-scale slumping of density  
 184 surfaces. The depth-integrated eddy energy is still advected by the depth average flow  $\bar{\mathbf{u}}^z$ , with westward propagation  
 185 at the long Rossby wave phase speed  $|c|$  (e.g., Chelton et al., 2011; Klocker and Marshall, 2014), diffused in the  
 186 horizontal (Grooms, 2015; Ni et al., 2020a,b) with eddy energy diffusivity  $\eta_E$ , dissipated at the rate  $\lambda$  ( $\lambda^{-1}$  is an eddy  
 187 energy dissipation time-scale, which can in principle vary in time and space; cf. Mak et al. 2022a; Torres et al. 2023;  
 188 Wilder et al. 2023), and  $E_0$  is a minimum eddy energy level. The parameterisation appears to be scale-aware in the  
 189 eddy energetics when splitting is employed, since the co-existing explicit eddy feedback affects the resolved mean-  
 190 state, and the resolved mean-state modifies the parameterised eddy feedback via changes in the parameterised eddy  
 191 energetics (Mak et al., 2023).

#### 192 2.4. Experimental set up

193 The model spin up follows the same procedure as that detailed in Ruan et al. (2023). The initial spun-up state  
 194 from a  $1^\circ$  resolution with a constant  $\kappa_{\text{gm}} = 1000 \text{ m}^2\text{s}^{-1}$  and a flat bottom, starting from model year  $-2300$  to year  
 195  $-300$  that already exists from Ruan et al. (2023) is interpolated onto the new domain and appropriately masked, and  
 196 at model year  $-300$  four sets of perturbation experiments were considered, running up to model year 0. We have  
 197 considered sample calculations where we spin-up from rest on the sloped domain; while there are differences in the  
 198 deeper parts of the ocean, over the top 700 m where we compute our bulk diagnostics the differences are minor (not  
 199 shown). For the perturbation experiments, a  $1/12^\circ$  horizontal resolution model (R12) resolving most of the mesoscale  
 200 eddies serves as a model truth as a reference. The primary focus here are the three eddy-permitting calculations at  
 201  $1/4^\circ$  horizontal resolution:

- 202 • R4, with no GM-based parameterisation active,
- 203 • SPLIT, with the GM-based GEOMETRIC parameterisation and with splitting (i.e., Eq. 5 and 6),
- 204 • GEOM, with the GM-based GEOMETRIC parameterisation but with no splitting (i.e., Eq. 5 and 6 without the  
 205 subscript  $L$ ; cf. Eq. 3-4 in Ruan et al. 2023).

206 For each of the experiments, a pre-industrial control scenario (assigned a suffix CTL) and an idealised climate change  
 207 scenario (assigned a suffix CC) are performed from model year 0 to 70. The pre-industrial control takes the standard  
 208 forcing as-is, while in the idealised climate change scenario the atmospheric pseudo-temperature has an added linear  
 209 trend of  $+0.04 \text{ }^\circ\text{C yr}^{-1}$  over the 70 model years, to mimic the SSP5-8.5 scenario in the North Atlantic (e.g., Tokarska  
 210 et al., 2020). All time-averaged diagnostics reported in this work are based on the last five years of the simulation  
 211 (spanning from the start of model year 66 and the end of model year 70).

212 The GEOMETRIC parameters are given in Table 1 and are the same in the SPLIT and GEOM calculations, with  
 213  $\alpha$  chosen to be closer to the recent works employing GEOMETRIC (Ruan et al., 2023; Mak et al., 2023; Wei et al.,  
 214 2024). The splitting procedure, where active, is performed every model day using the procedure detailed in Mak  
 215 et al. (2023): briefly, a diffusion based filter in space with a pre-defined length-scale  $L$  (taken to be 100 km here) is  
 216 performed per model level, where the filtering kernel is closely related to the Matérn auto-covariance (e.g., Whittle,  
 217 1963; Lindgren et al., 2018). Fig. 1a shows the bathymetry and the resulting  $f/H$  contours (that the geostrophic flow  
 218 should be constrained somewhat to follow), noting the poleward deflection of the contours as we move eastwards from  
 219 the western boundary. A sample output from SPLIT is given in Fig. 1b-d for a snapshot of the sea surface temperature,  
 220 showing the total, filtered and residual field respectively, demonstrating that the splitting procedure leaves a portion  
 221 of the explicit fluctuations intact, as seen in the residual field. The analogous results in R12, GEOM and R4 have  
 222 been omitted here for brevity: R12 and R4 permits explicit fluctuations, while GEOM largely resembles the coarse  
 223 resolution calculations (cf. Ruan et al., 2023; Mak et al., 2023).

224 In Fig. 2 we show the resulting  $\kappa_{\text{gm}}(x, y)$  field for both SPLIT and GEOM. Both are large in the Western Boundary  
 225 Current region, because of large simulated total parameterised eddy energy  $E$ . Notice that values of  $\kappa_{\text{gm}}$  are much

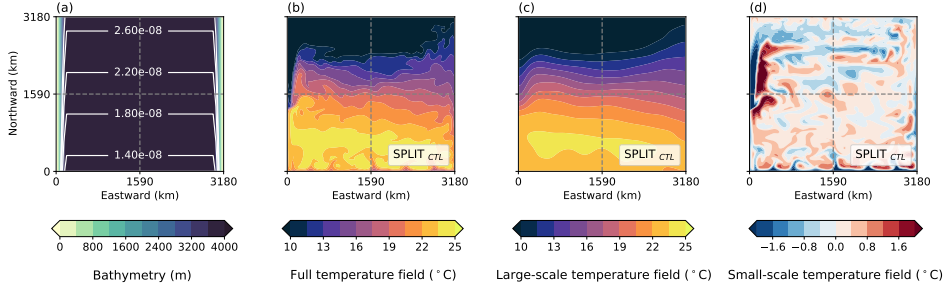


Figure 1: (a) Model bathymetry (shading) and the large-scale potential vorticity contours as  $f/H$  ( $\text{m}^{-1}\text{s}^{-1}$ ) in the present model, where  $f$  is the Coriolis parameter and  $H$  is the depth. The diagnosed surface temperature field ( $^{\circ}\text{C}$ ) from SPLIT, showing (b) the full temperature field, (c) the associated large-scale temperature field, and (d) residual or small-scale temperature field.

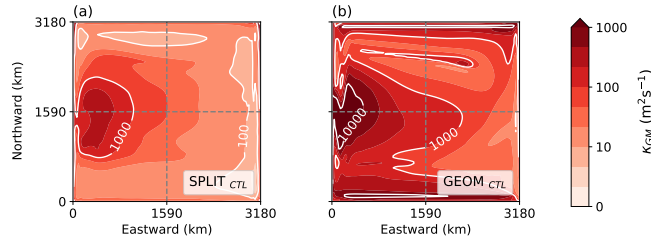


Figure 2: The resulting  $\kappa_{\text{gm}}(x, y)$  ( $\text{m}^2\text{s}^{-1}$ ) distribution from (a) SPLIT and (b) GEOM, with some representative contours of  $\kappa_{\text{gm}}$  marked on.

226 more modest in SPLIT than in GEOM (domain-averaged value at 468 and 2361  $\text{m}^2\text{s}^{-1}$  respectively), given the same  
 227 parameter choices. While the reduction in the horizontal gradients of the associated filtered density field  $\rho_L$  does  
 228 lead to a reduction of the simulated  $E$  (by affecting  $\kappa_{\text{gm}}$ ), a fundamental difference leading to non-damping of explicit  
 229 eddies is that the eddy-induced velocity  $\mathbf{u}_L^*$  is a large-scale rather than grid-scale object. The reported behavior later  
 230 is found to crucially depend on the use of  $\mathbf{u}_L^*$  (i.e., splitting), and less on a reduction in  $\kappa_{\text{gm}}$  (which can be achieved by  
 231 tuning  $\alpha$  and/or  $\lambda$ ).

232 One point we make is that, since we have a non-trivial bathymetry in the present model set up, it might be  
 233 possible that a tapering of the GM coefficient  $\kappa_{\text{gm}}$  is required over continental slopes, where the dynamics of eddies  
 234 and topographic effects can differ from the open ocean (e.g., LaCasce and Brink, 2000; Stewart and Thompson, 2013;  
 235 Wang and Stewart, 2018). The present implementation of GEOMETRIC in NEMO takes a simple choice of tapering  
 236  $\kappa_{\text{gm}}$  to zero as the Rossby deformation becomes sufficiently small, which in the present model is largely dictated by  
 237 the modelled water depth. Simulations with and without tapering in the present model (enabled by commenting out  
 238 the relevant lines of the source code) seem to make no qualitative difference to any of our reported results. There  
 239 are more advanced choices based on slope parameters or Burger numbers that have shown promise (e.g., Wei et al.,  
 240 2022, 2024; Nummelin and Isachsen, 2024), which may affect the model response, although we have not considered  
 241 implementations of those procedures here. The present reported results do not have the Rossby number based tapering  
 242 of  $\kappa_{\text{gm}}$  deactivated.

### 243 3. Pre-industrial control responses

#### 244 3.1. Physical responses

245 We first show some metrics relating to the modelled circulation associated with the set of calculations. In Fig. 3  
 246 we show the barotropic streamfunction  $\Psi_{\text{baro}}$ , calculated as

$$\Psi_{\text{baro}} = \int_{\tilde{x}=0}^{\tilde{x}=x} \int_{-H}^0 \bar{v}(\tilde{x}, y, z) dz d\tilde{x}. \quad (7)$$



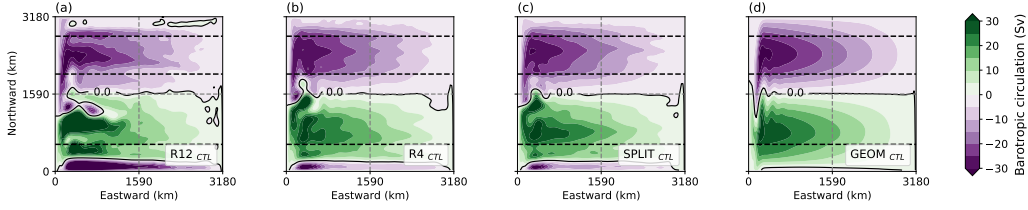


Figure 3: The barotropic streamfunction  $\Psi_{\text{baro}}$  (in  $\text{Sv} = 10^6 \text{ m}^3 \text{ s}^{-1}$ ) of (a) R12, (b) R4, (c) SPLIT, and (d) GEOM, with the zero contour added. The black dashed lines represent the sample latitudinal cross sections  $S_{1,2,3}$  going from south to north.

247 The streamfunction  $\Psi_{\text{baro}}$  displays the basic features of a subtropical gyre to the south and a subpolar gyre to the  
 248 north, separated by a Western Boundary Current region. Compared to the analogous diagnostic reported in Fig. 2 in  
 249 Ruan et al. (2023), a main difference here is in the poleward deflection of the subpolar gyre as we move away from the  
 250 western boundary, consistent with the presence of the sloping bathymetry (e.g., Jackson et al., 2006). The R12, R4 and  
 251 SPLIT calculations all show some explicit representation of a Western Boundary Current as well as some semblance  
 252 of fluctuations even in the time-averaged data, unlike the GEOM calculation, which largely resembles the coarse  
 253 resolution calculations (cf. Ruan et al., 2023, Fig. 2b). Examination of the eddy kinetic energy field or snapshots  
 254 of surface relative vorticity field indicates that the GEOM calculations possess very weak fluctuations for the present  
 255 choice of parameter values, relative to the R4 and SPLIT calculations (not shown). We note that the R12 Western  
 256 Boundary Current is still slightly south of the latitudinal center line even though the zonal wind stress is symmetric  
 257 about the latitude centre line, and extends more eastward (cf. Fig. 3a here, and Fig. 2a of Ruan et al. 2023 for R12).  
 258 Moreover, all calculations display some representation of the re-circulating Fofonoff gyres towards the northern and  
 259 southern boundary, although the northern one is somewhat weaker, presumably due to the presence of the non-trivial  
 260 bathymetry in this work.

261 A subtlety in this work is that the eddy-permitting calculations do have a representation of the Western Boundary  
 262 Current in some way (at least for R4 and SPLIT), affecting the size of what would be identified as the subpolar gyre.  
 263 While the works of Couespel et al. (2021) and Ruan et al. (2023) focus on the analysis within the subpolar gyre  
 264 (defined over fixed geographical locations) primarily because it is the most bio-active region in the modelled domain,  
 265 in this work we consider the whole domain but exclude the Fofonoff gyres as the analysis region when computing  
 266 averaged/integrated quantities. For computing fluxes, we consider the cross sections at  $y = 25^\circ$  and  $45^\circ$  N marked on  
 267 as black dashed lines in the figures as appropriate (denoted  $S_{1,3}$ ), roughly as the southern boundary of the subtropical  
 268 gyre, and the northern boundary of the subpolar gyre respectively. For completeness, we also mark on and compute  
 269 fluxes over the  $y = 38^\circ$  N section (denoted  $S_2$ ), which is an empirically determined location that is sufficiently north  
 270 of the simulated Western Boundary Current (see Fig. 4a-d), for reasons to be elaborated on later. The analysis region  
 271 of primary interest is the region bounded in the horizontal by  $S_1$  and  $S_3$ , and in the vertical by  $z = -700$  m; we neglect  
 272 the deeper parts of the ocean since these regions would presumably not have equilibrated within the 70 model year  
 273 period we are considering.

274 As another measure of the circulation, we show in Fig. 4 the residual meridional overturning circulation (MOC)  
 275 streamfunction  $\Psi_{\text{MOC}}$ , diagnosed as

$$\Psi_{\text{MOC}} = \int_{\tilde{z}=-H}^{\tilde{z}=\tilde{z}} \int_0^{L_x} \bar{v}(x, y, \tilde{z}) + v^*(x, y, \tilde{z}) \, dx \, d\tilde{z}, \quad (8)$$

276 as well as a histogram of the yearly maximum mixed layer depth (identified as the first depth below which  $|\sigma_\theta(z) -$   
 277  $\sigma_\theta(z = -10 \text{ m})| > 0.01$ , where  $\sigma_\theta$  is the potential density referenced to sea level) in the deep water formation region,  
 278 between  $y = 45^\circ$  N and the northern boundary (i.e., the region north of  $S_3$ ). We observe that  $\Psi_{\text{MOC}}$  displays a structure  
 279 consistent with previous works of the double-gyre configuration (Couespel et al., 2021; Ruan et al., 2023). Relative  
 280 to the model truth R12, the R4 calculation has a rather large positive bias in the subpolar gyre region (Fig. 4b) and  
 281 deep bias in the mixed layer (Fig. 4f), while the GEOM calculation has the converse (Fig. 4d, h). The observations  
 282 are consistent with the expectation that the explicit eddy-mean interaction is too weak in R4, leading to a mixed layer  
 283 that is too deep (since eddies are not able to counter the deepening of the mixed layer as much) and a MOC that is too

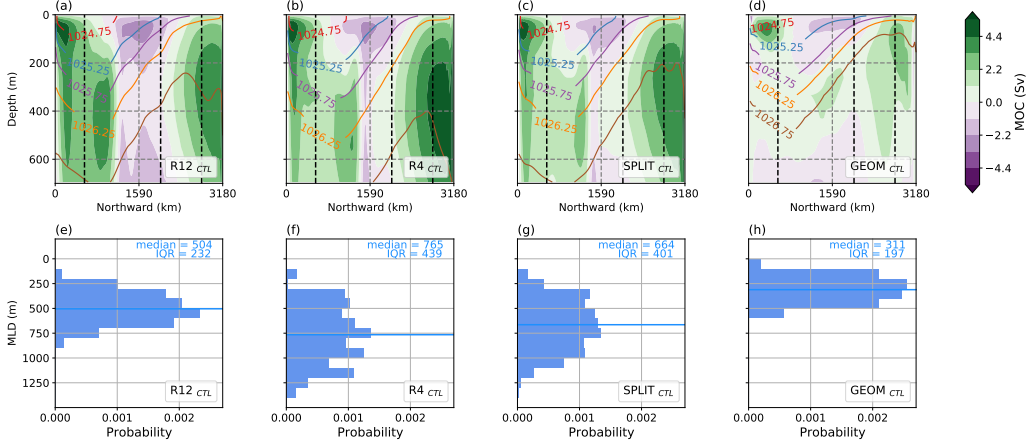


Figure 4: (Top row) The Meridional Overturning Circulation streamfunction  $\Psi_{\text{MOC}}$  (shading, in  $\text{Sv} = 10^6 \text{ m}^3 \text{ s}^{-1}$ ) and lines of constant potential density referenced to sea level (contours, in  $\text{kg m}^{-3}$  with  $0.5 \text{ kg m}^{-3}$  interval, for (a) R12, (b) R4, (c) SPLIT, and (d) GEOM. The black dashed lines represent the sample latitudinal cross sections  $S_{1,2,3}$  going from south to north. (Bottom row) The histogram of yearly maximum mixed layer depth distributions ( $m$ ), identified as the first depth below which  $|\sigma_\theta(z) - \sigma_\theta(z = -10 \text{ m})| > 0.01$  where  $\sigma_\theta$  is the potential density referenced to sea level, with 20 bins ranging from 0 – 1500 m) and median (indicated by horizontal blue line) over the northern area where deep water formation occurs, for (e) R12, (f) R4, (g) SPLIT, and (h) GEOM; the median and inter-quartile range (IQR) is shown (in units of  $m$ ), and the axes of the histograms have been flipped for convenient visual comparison.

284 strong. In GEOM the parameterised eddies lead to a response going too far the other way, leading to too shallow a  
 285 mixed layer and too weak a MOC, reminiscent of the coarse resolution calculations reported in Fig. 3 and 4 of Ruan  
 286 et al. (2023). However, we note that GEOM possesses a distribution in the mixed layer depth that is closer to R12,  
 287 although there is a shallow bias.

288 The use of splitting appears to reduce the associated biases in the MOC and the distribution of sample isopycnals  
 289 as seen in Fig. 4c, and reduce the deep biases of the mixed layer somewhat as seen in Fig. 4f (although the distribution  
 290 is still rather wide compared to the distribution of the model truth in Fig. 4e). More quantitatively, the area-weighted  
 291 average root-mean-square mismatch to R12 within the whole domain is of 1.21, 1.09, and 1.98 Sv in R4, SPLIT, and  
 292 GEOM respectively. The median of the maximum mixed layer depth north of  $S_3$  is 504, 765, 664 and 311 m, and the  
 293 inter-quartile range is 232, 439, 401 and 197 m respectively.

294 One consequence of biases in the MOC is reflected in the ocean heat transports, diagnosed as

$$\text{OHT} = \rho_0 C_p \int_{z=-700}^{z=0} \int_{x=0}^{x=L_x} \overline{\mathbf{u} \Theta} \, dx \, dz = \rho_0 C_p \int_{z=-700}^{z=0} \int_{x=0}^{x=L_x} \overline{(\bar{\mathbf{u}} + \mathbf{u}' + \mathbf{u}^*) (\bar{\Theta} + \Theta')} \, dx \, dz, \quad (9)$$

295 where  $\rho_0$  is reference density at  $1026 \text{ kg m}^{-3}$ ,  $C_p = 3991.86 \text{ J K}^{-1}$  is the heat capacity, and  $\Theta$  would be the  
 296 Conservative Temperature (although we use a linear equation of state here). Fig. 5 shows the *total* meridional heat  
 297 transport and vertical transport, zonally and vertically integrated over the top 700 m; we neglect the deeper parts of  
 298 the ocean since these regions have not equilibrated within the 70 model year period we are considering. We note that  
 299 the dominant contribution to the transports shown in Fig. 5 is from the *mean* component  $\bar{\mathbf{u}} \bar{\Theta}$ . However, while the  
 300 eddy components are subdominant in the overall transport, they are absolutely crucial for shaping the mean state and  
 301 impacting  $\bar{\mathbf{u}} \bar{\Theta}$ .

302 The diagnosed meridional heat transport is mostly towards the north in the analysis region (within  $S_1$  and  $S_3$ )  
 303 and peaks near the Western Boundary Current (Fig. 5a). Relative to the model truth R12, R4 and GEOM possess a  
 304 meridional heat transport that is too strong and too weak respectively, while SPLIT is much closer to model truth;  
 305 quantitatively, the area-weighted average northward heat transport is 3.89, 7.29, 4.41, and  $-0.41$  PW respectively for  
 306 R12, R4, SPLIT and GEOM in the analysis domain<sup>2</sup>. The improvements appear to come from a better representation

<sup>2</sup>Note the values in Ruan et al. (2023) are smaller, because those are integrated over the whole domain depth. This was an inconsistent choice on our part.

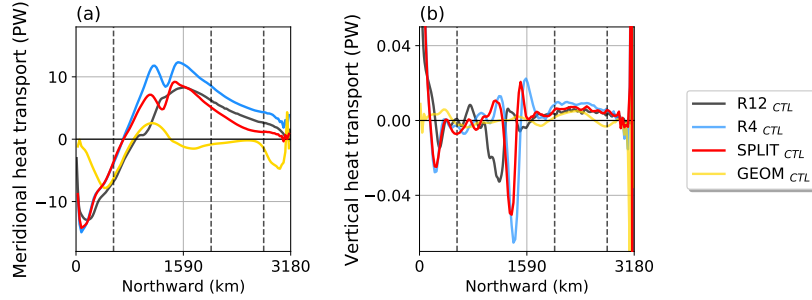


Figure 5: Total (mean and eddy) heat transport (in units of  $\text{PW} = 10^{15} \text{ W}$ ), integrated zonally and vertically over the top 700 m, for model truth (R12, black line) and eddy-permitting simulations (R4, blue line; SPLIT, red line; GEOM, yellow line). (a) Meridional heat transport  $\overline{v\Theta^x}$ , positive values denoting northward transport. (b) Vertical heat transport  $\overline{w\Theta^x}$ , positive values denoting upward transport. The black dashed lines represent the sample latitudinal cross sections  $S_{1,2,3}$  going from south to north. We make a note that the values here are the transports integrated over the top 700 m, and are larger than the analogous values in Ruan et al. (2023), where the associated transports are integrated over the whole model depth; that former was a inconsistent choice on our part.

of the stratification, which impacts both the transport and the heat content distribution.

For the vertical heat transport, there is a notable region with strong downward heat transport corresponding to the location of the Western Boundary Current (cf. Fig. 5b). The local biases between R12 with R4 and SPLIT are from the Western Boundary Current separating at a different latitude (there is almost no explicit representation as such in the GEOM case). The observation is partly the reason for the choice of a sample section  $S_2$  at  $y = 38^\circ \text{ N}$  to be sufficiently away from the model Western Boundary Current, so that the associated section possesses a dynamical regime that is more comparable. Nevertheless, we can see that the magnitude of vertical heat transports of SPLIT is less than that of R4 over most of the region, and seems to be visually closer to the model truth than GEOM. Quantitatively, the area-weighted average *upward* heat transport over the analysis region is 2.76, 5.74, 4.24 and  $1.15 \times 10^{-3} \text{ PW}$  respectively for R12, R4, SPLIT and GEOM, while the analogous *downward* heat transport is 3.44, 4.63, 3.39 and  $0.84 \times 10^{-3} \text{ PW}$  (the total heat transport is a small residual of the two, and is negative for R12). The key observation here is that the associated values for SPLIT are closer to the model truth R12, smaller than R4, and larger than that GEOM, consistent with our theoretical expectations.

### 3.2. Biogeochemical responses

Given the improvements to the physical responses in SPLIT achieved by employing the GEOMETRIC parameterisation with the splitting procedure, we might expect to observe related improvements in the biogeochemical responses. We focus on nitrate ( $\text{NO}_3^-$ ), which contributes primarily to the NPP in the present set up (e.g., Couespel et al., 2021; Ruan et al., 2023). The improvement in the biogeochemistry response can be seen from an improvement to the resulting nitrate distributions. The nitraclines, which largely mimics the isopycnal distribution since we expect transport to be constrained to along-isopycnal directions under the geostrophic assumption, is closer in SPLIT to the model truth (not shown for brevity, but see Fig. 4a-d for isopycnal distribution; cf. Ruan et al. 2023, Fig. 3a-c and Fig. 6a-c). The area-weighted average of  $\text{NO}_3^-$  within the analysis domain are 12.02, 11.49, 11.81, and  $10.55 \text{ mmol N m}^{-3}$  respectively for R12, R4, SPLIT and GEOM (where N is the nitrogen currency), demonstrating an improvement of SPLIT over R4 and GEOM in a way that is consistent with our expectations.

In Fig. 6 we show diagnostics related to the vertically integrated Net Primary Production (NPP; in units of  $\text{mmol N m}^{-2} \text{ day}^{-1}$ ). Fig. 6a shows the distribution in the horizontal, and only the R12 simulation is shown since the general pattern of productive subpolar and oligotrophic subtropical gyre is similar in the eddy-permitting simulations. Fig. 6b shows the zonally averaged latitudinal distribution of the same quantity but over the set of calculations. Both R4 and SPLIT capture the general shape of the distribution for the R12 calculation, while the GEOM calculation is too small in general, consistent with results from coarse resolution calculations (e.g., Fig. 5 of Ruan et al., 2023). Although the diagnosed NPP is weaker in SPLIT compared to R4 in the subpolar gyre region, the overshoot in the Western Boundary Current region is alleviated in SPLIT and is closer to the R12 model truth. Quantitatively, over

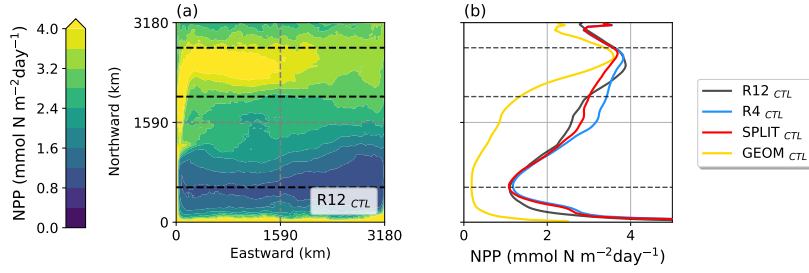


Figure 6: Vertically integrated Net Primary Production (NPP,  $\text{mmol N m}^{-2} \text{day}^{-1}$ , where N is the nitrogen currency). (a) Horizontal distribution for R12, and the distribution pattern in other simulations (R4, SPLIT, GEOM) is similar and thus is omitted. (b) The zonally averaged latitudinal distribution of vertically integrated NPP, for the model truth (R12, black line) and eddy-permitting simulations (R4, blue line; SPLIT, red line; GEOM, yellow line). The black dashed lines represent the sample latitudinal cross sections  $S_{1,2,3}$  going from south to north.

339 the analysis region, the area-weighted average NPP is 2.64, 2.83, 2.61, and 1.31  $\text{mmol N m}^{-2} \text{day}^{-1}$  respectively  
 340 for R12, R4, SPLIT and GEOM. The diagnosed NPP for R4 and GEOM is too large and too small respectively, and  
 341 SPLIT results in a much closer NPP to the model truth. The results in the biogeochemical response are consistent with  
 342 our expected and diagnosed physical response, so there is evidence that we are getting an improved biogeochemical  
 343 response because of a better physical response (cf. a case reported in Ruan et al. 2023, where one could obtain a  
 344 reasonable biogeochemical response without necessarily having a consistent physical response).

345 Similar to the previous studies of Couespel et al. (2021) and Ruan et al. (2023), we diagnose the nitrate fluxes  
 346 from advective and/or diffusive processes. The total nitrate advection is given by  $\nabla \cdot (\mathbf{u}N)$ , where  $N$  denotes the nitrate  
 347 concentration, and by the divergence theorem, the total supply in and out of the analysis region is expressed by

$$\int_{\text{domain}} \nabla \cdot \overline{\mathbf{u}N} \, dx \, dy \, dz = \left( \int_{S_1} + \int_{S_3} \right) \overline{vN} \, dx \, dz + \int_A \overline{wN} \, dx \, dy, \quad (10)$$

348 where  $A$  is the horizontal area between  $S_1$  and  $S_3$  at fixed height  $z = z_0$ , and we assume there is no surface input of  $N$ .  
 349 The contributions can further be decomposed into explicit and parameterised eddy components as in Eq. 9. In Fig. 7  
 350 we show the *total* nitrate fluxes, where the vertical flux is diagnosed by performing a horizontal integral (panel a),  
 351 while the meridional fluxes across  $S_{1,2,3}$  are the zonal integral over  $S_{1,2,3}$  that are then *cumulatively* integrated in the  
 352 vertical (panels b, c, d). We note that while the *total* is shown, the dominant contribution is from the *mean* component  
 353  $\overline{vN}$  and  $\overline{wN}$ , rather than from the *eddy* component (explicit and/or parameterised), consistent with the previous results  
 354 reported in Couespel et al. (2021) and Ruan et al. (2023). Vertical diffusion is large over the top 50 m or so, while  
 355 lateral diffusion is of secondary importance over all depths (not shown). Again, while the eddy contribution to tracer  
 356 transport may be of secondary importance, the eddies are crucial in shaping the mean stratification, which ends up  
 357 dictating the overall large-scale supply of nitrate.

358 The nitrate advection profiles of R4 and SPLIT agree reasonably well with R12, with SPLIT being generally of  
 359 smaller magnitude than R4, and certainly an improvement on GEOM (and analogous coarse resolution calculations,  
 360 such as those in Fig. 7 of Ruan et al. 2023). The main difference appears in the vertical nitrate supply in Fig. 7a,  
 361 where the vertical supply of R4 and SPLIT are too small near the upper parts of the modelled ocean (and, interestingly,  
 362 the diagnosed values of GEOM agree better with R12 here), while they are larger at the deeper regions. The smaller  
 363 supply of nitrate particularly in the vertical, is presumably the dominant contribution to why the NPP in SPLIT is  
 364 smaller than R4, and closer to that of the model truth R12.

365 A final comment we make is that there are large differences in the associated meridional transport if  $S_2$  is within  
 366 the explicitly represented Western Boundary Current. For comparison reasons, we chose  $S_2$  to be north of all the  
 367 explicitly represented Western Boundary Currents across the set of simulations, and somewhere near the southern  
 368 boundary of the modelled subpolar gyre. While it may be possible to compute the flux across some contour related to  
 369 the Western Boundary Current defined dynamically, for simplicity reasons we have opted to simply choose a sample  
 370 section to provide a representative diagnostic.

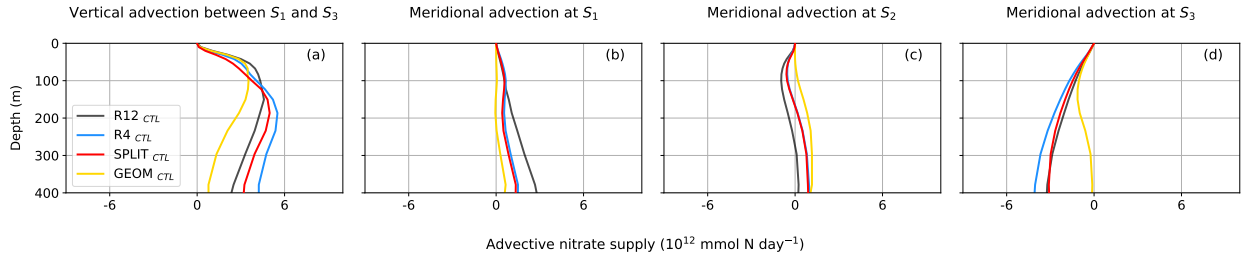


Figure 7: Total advective nitrate supply ( $\text{mmol N day}^{-1}$ , where N is the nitrogen currency unit) for the model truth (R12, black line) and eddy-permitting simulations (R4, blue line; SPLIT, red line; GEOM, yellow line). (a) The vertically varying vertical advective supply horizontally integrated. (b, c, d) The meridional advective contribution as a *cumulative* vertical integral at sample sections  $S_{1,2,3}$ . The contribution at  $S_3$  is calculated with an extra minus sign, so negative values in panel d indicate a flux out of the analysis region. Also note that in panel c the blue line overlaps with the red line.

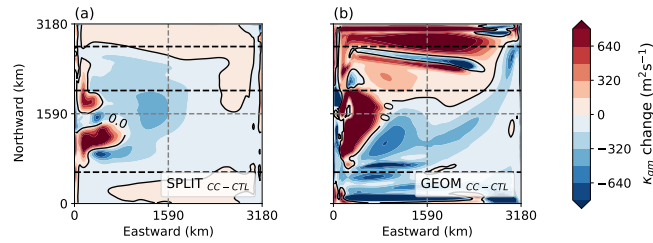


Figure 8: Raw difference of the  $\kappa_{\text{gm}}(x, y)$  ( $\text{m}^2\text{s}^{-1}$ ) distribution between the climate change scenario and the control scenario (see Fig. 2) for (a) SPLIT, and (b) GEOM. The black dashed lines represent the sample latitudinal cross sections  $S_{1,2,3}$  going from south to north.

#### 371 4. Noteworthy characteristics of the sensitivities under idealised climate change

##### 372 4.1. Physical responses

373 In the previous work of Ruan et al. (2023) we investigated the performance of GEOMETRIC under idealised  
 374 climate change scenarios for coarse resolution models, and found that the use of GEOMETRIC improved on the  
 375 sensitivities, at least compared to the standard GM scheme with a constant  $\kappa_{\text{gm}}$ . We perform a similar set of  
 376 calculations under the same idealised climate change scenario detailed in §2.4 to investigate the responses between  
 377 the eddy-permitting models R4, SPLIT and GEOM.

378 Fig. 8 shows the raw difference of  $\kappa_{\text{gm}}(x, y)$  between the climate change and control case (cf. Fig. 2) for SPLIT  
 379 and GEOM. The change in  $\kappa_{\text{gm}}$  mainly appears near the Western Boundary Current region and the northern boundary,  
 380 and is relatively modest for SPLIT compared to GEOM, because it is the large-scale filtered stratification that is used  
 381 in the calculation of the parameterised total eddy energy (i.e., Eq. 5 and 6). The change in  $\kappa_{\text{gm}}$  in GEOM is large  
 382 in the deep water forming region towards the northern boundary, consistent with but larger in magnitude than the  
 383 corresponding result in Fig. 8b of Ruan et al. (2023) for the coarse resolution calculation. As reported previously in  
 384 Ruan et al. (2023), this significant increase in  $\kappa_{\text{gm}}$  in the deep water formation region affects the mixed layer depth  
 385 and extent of deep water formation, which affects the overall stratification in the domain, impacting the meridional  
 386 overturning circulation.

387 Fig 9a-d shows the raw difference between the meridional overturning streamfunction  $\Psi_{\text{MOC}}$  under the climate  
 388 change and control scenario, while Fig 9e-f shows the histogram of the yearly maximum mixed layer depth  
 389 distributions under both scenarios (cf. Fig. 4). Overall, the overturning circulation weakens and the mixed layer  
 390 depth shoals, consistent with the results from the previous works of Couespel et al. (2021) and Ruan et al. (2023).  
 391 Note that the change of  $\Psi_{\text{MOC}}$  in R12 is somewhat different to that reported in Fig. 9a of Ruan et al. (2023): the  
 392 strength in the subtropical gyre here *decreases*, while it *increases* in the previous works, presumably related to the  
 393 presence of the non-trivial bathymetry in this work. The alternating positive-negative pattern near the centre of the

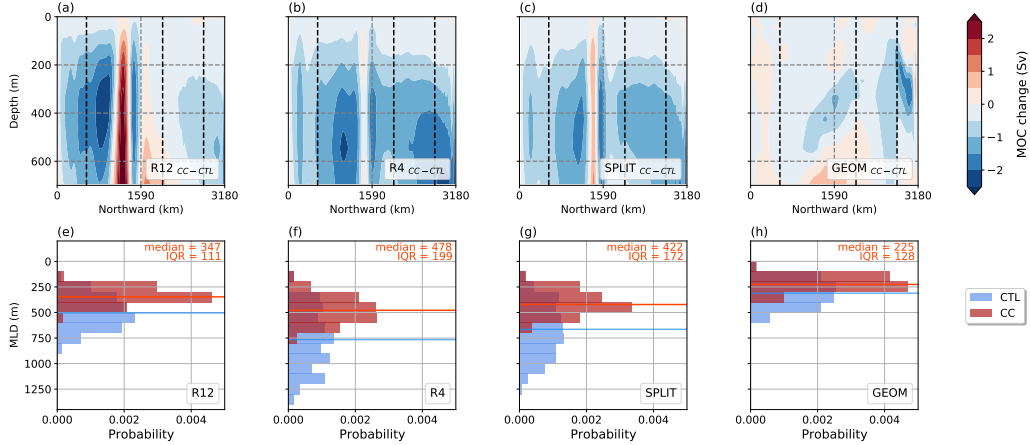


Figure 9: (Top row) Raw difference of the meridional overturning streamfunction  $\Psi_{\text{MOC}}$  ( $\text{Sv} = 10^6 \text{ m}^3 \text{ s}^{-1}$ ) between the climate change and the control scenario (Fig. 4a-d), for (a) R12, (b) R4, (c) SPLIT, and (d) GEOM; negative values largely indicate a weakening of the overturning strength. The black dashed lines represent the sample latitudinal cross sections  $S_{1,2,3}$  going from south to north. (Bottom row) The histogram of yearly maximum mixed layer depth distributions ( $m$ ), identified as the first depth below which  $|\sigma_\theta(z) - \sigma_\theta(z = -10 \text{ m})| > 0.01$  where  $\sigma_\theta$  is the potential density referenced to sea level, with 20 bins ranging from 0 – 1500 m) and median (indicated by the horizontal line) over the area where deep water formation occurs, for the climate change scenario (in red) and control scenario (in blue, see Fig. 4e-h), for (e) R12, (f) R4, (g) SPLIT, and (h) GEOM; the median and inter-quartile range (IQR) is shown (in units of  $m$ ), and the axes of the histograms have been flipped for convenient visual comparison.

394 domain corresponds to a shift of the Western Boundary Current northwards (corresponding to a shift in the purple  
 395 pattern in Fig. 4a). We note that the shift in the Western Boundary Current as seen in  $\Psi_{\text{MOC}}$  is more noticeable  
 396 in SPLIT. The decrease in the subpolar gyre is less in SPLIT relative to R4 and closer to R12 visually, although R4  
 397 possesses a change in the subtropical gyre that is closer to R12. R4 and SPLIT still have a slightly deep bias in the  
 398 mixed layer, but overall the shift is not unreasonable compared to R12. By contrast, GEOM has a weak change in the  
 399  $\Psi_{\text{MOC}}$ , but only because the control  $\Psi_{\text{MOC}}$  in Fig. 4d is already rather small. Additionally, the mixed layer in GEOM  
 400 is too shallow, as expected from the strong increase in  $\kappa_{\text{gm}}$  in the deep water forming region, consistent with results  
 401 from Ruan et al. (2023).

402 The changes in both the meridional and vertical heat transport are consistent with the observed changes in  $\Psi_{\text{MOC}}$ ,  
 403 and are perhaps best quantified by simply stating the diagnosed values averaged with the analysis region. The  
 404 area-weighted averaged northward heat transport is 4.67, 5.05, 3.17 and 0.56 PW for R12, R4, SPLIT and GEOM  
 405 respectively. In this setting, the diagnosed northward heat transport for R4 is now closer to R12 than that of SPLIT.  
 406 Similarly, the total upward heat transport is 3.41, 6.46, 5.40 and  $1.07 \times 10^{-3}$  PW for R12, R4, SPLIT and GEOM  
 407 respectively, while for downward heat transport is 3.18, 4.96, 4.35 and  $1.12 \times 10^{-3}$  PW; the values for SPLIT are more  
 408 consistent with R12 and smaller in magnitude than R4 as expected. Note however the sensitivities of the meridional  
 409 and vertical heat transports of both R4 and SPLIT between climate change and control scenarios differ in magnitude  
 410 and sometimes in sign (see Table 2), suggesting improvements to the sensitivities relative to the R12 model truth  
 411 requires further investigation.

#### 412 4.2. Biogeochemical responses

413 In Fig. 10 we show diagnostics in relation to the vertically integrated NPP. Fig. 10a shows the horizontal  
 414 distribution of the raw difference between climate change and control scenario for R12, where we see there is an  
 415 overall decline of NPP, in line with results from Couespel et al. (2021) and Ruan et al. (2023). Minor differences in  
 416 the Western Boundary Current region arise compared to previous works, presumably because of the presence of the  
 417 non-trivial bathymetry leading to a different representation of the circulation (e.g. Fig. 11a of Ruan et al. 2023). The  
 418 corresponding figures for the eddy-permitting calculations have been omitted because the changes are qualitatively  
 419 similar. Fig. 10b shows the analogous zonally averaged diagnostic across the set of experiments. We see that the  
 420 decrease near the Western Boundary Current in SPLIT matches better with R12, and both SPLIT and R4 perform

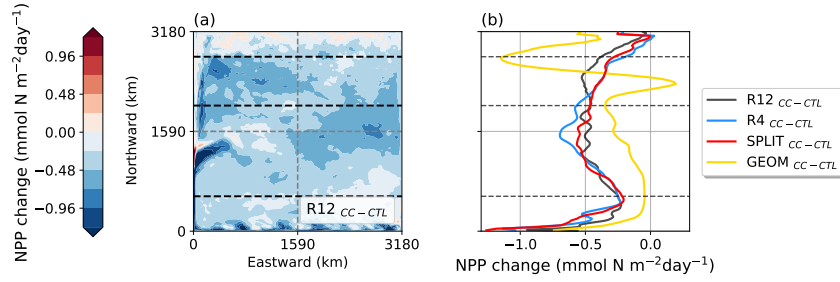


Figure 10: Raw difference of the vertically integrated Net Primary Production (NPP,  $\text{mmol N m}^{-2} \text{day}^{-1}$ , where N is the nitrogen currency) between the climate change scenario and the corresponding control scenario (see Fig. 6a). (a) Horizontal distribution for R12; the distribution pattern is similar for the eddy-permitting simulations and have been omitted. (b) The zonally averaged latitudinal distribution for model truth (R12, black line) and eddy-permitting simulations (R4, blue line; SPLIT, red line; GEOM, yellow line). The black dashed lines represent the sample latitudinal cross sections  $S_{1,2,3}$  going from south to north.

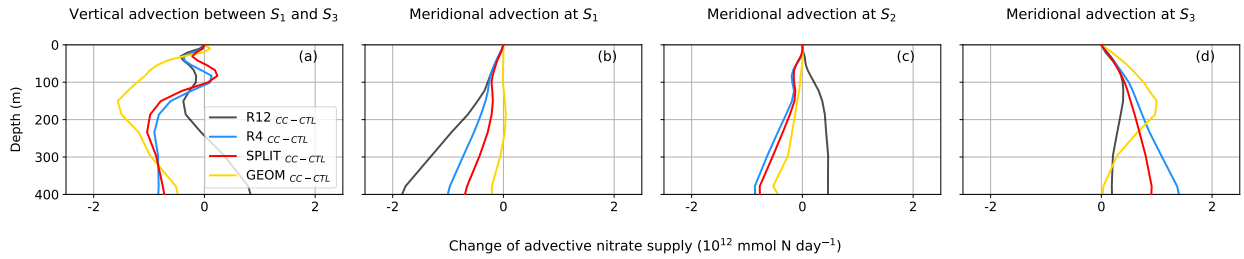


Figure 11: Raw difference of the total advective nitrate supply ( $\text{mmol N day}^{-1}$ , where N is the nitrogen currency unit) into the analysis domain between the climate change scenario and the corresponding control scenario (see Fig. 7) for model truth (R12, black line) and eddy-permitting simulations (R4, blue line; SPLIT, red line; GEOM, yellow line). (a) The vertically varying vertical advective supply horizontally integrated. (b – d) The meridional advective contribution as a cumulative vertical integral at sample sections  $S_{1,2,3}$ . The contribution at  $S_3$  is calculated with an extra minus sign, so that positive values here indicate a *positive* supply (or decrease in the flux out of the analysis domain).

421 similarly in the subpolar gyre, both with a positive bias. The GEOM calculation displays substantial sensitivity in the  
 422 subpolar gyre, because of the significant change in  $\kappa_{\text{gm}}$  (Fig. 8b), analogous to the sensitivity reported in Ruan et al.  
 423 (2023). The overall sensitivity within the analysis domain between R12, R4 and SPLIT are not significantly different.  
 424 Quantitatively, the area-weighted vertically integrated NPP is 2.18, 2.36, 2.18 and 1.07  $\text{mmol N m}^{-2} \text{day}^{-1}$ , with  
 425 a corresponding percentage difference of  $-17.2\%$ ,  $-16.5\%$ ,  $-16.6\%$ , and  $-18.3\%$  for R12, R4, SPLIT and GEOM  
 426 respectively. While the SPLIT experiment arguably displays a better agreement with R12, the R4 experiment performs  
 427 reasonably (and certainly better than GEOM in the present eddy-permitting regime).

428 In Fig. 11 we show the raw difference between the vertical advective nitrate supply and the meridional advective  
 429 nitrate supply over the vertical planes  $S_{1,2,3}$  (cf. Fig. 7). In general, the vertical nitrate supply and meridional nitrate  
 430 supply in  $S_{1,2}$  decreases, but increases in  $S_3$  (which because of the minus sign corresponds to a *negative* supply  
 431 or positive flux out of the analysis domain), related to a weakening of the overturning circulation (cf. Fig. 9a-d).  
 432 There is however a general disagreement in terms of the changes in the advective contributions in the eddy-permitting  
 433 calculations with R12, which is in contrast to the coarse resolution results reported in Fig. 13 of Ruan et al. (2023).  
 434 This could be due to the presence of bathymetry in the present model, but also could be that the statement “a GM-based  
 435 parameterization turns an eddy-permitting model into an expensive coarse resolution model” as we have hypothesised  
 436 is overly simplified. While the overall integrated response of the SPLIT calculation appears to be reasonable relative  
 437 to the model truth, further investigations and/or proposal for improvements are warranted in due course.

## 438 5. Conclusions and discussions

439 With increasing computational power, eddy-permitting ocean models that can partially resolve mesoscale eddies  
440 become increasingly feasible, and are tractable targets for the next generation of Earth System Models. While it is  
441 known that such models offer some benefits in reducing biases (e.g., Fox-Kemper et al., 2019; Hewitt et al., 2020;  
442 Beech et al., 2022), it is also known that the eddy-mean interaction are somewhat misrepresented, and some degree of  
443 mesoscale eddy parameterisation may still be beneficial. Our work here contributes to the examination of the effect  
444 of different ways of representing the eddy-mean interaction on the associated model physical and biogeochemical  
445 response in an idealised double-gyre model, based on the model and experiment set up from the related previous  
446 works (Couespel et al., 2021; Ruan et al., 2023). A difference in the model set up compared with the previous works  
447 is that we employ a non-trivial bathymetry, with a slope on the west and east sides (Jackson et al. 2006; cf. Eq. 4  
448 and Fig. 1a). The qualitative conclusions we draw from this work are however robust also in the absence of model  
449 bathymetry (not shown).

450 We focus our attention on examining a new way of employing a Gent–McWilliams (GM) scheme (Gent and  
451 McWilliams, 1990; Gent et al., 1995) in eddy-permitting ocean models, termed *splitting* in the previous work of Mak  
452 et al. (2023), to the present double-gyre system. Focusing on the GM-based version GEOMETRIC (Marshall et al.,  
453 2012; Mak et al., 2022b), we compare model responses of a model employing GEOMETRIC with splitting against  
454 model responses in an eddy-rich model truth, and eddy-permitting cases where no GM-based parameterisation is  
455 employed, and where a GM-based scheme is used as-is. We expect that in the case with no parameterisation, the  
456 modelled stratification will be too deep and the meridional overturning circulation too strong, because the represented  
457 eddy-mean interaction in an eddy-permitting calculation is too weak. As a consequence, the modelled heat transports  
458 and biogeochemical response in the net primary production (NPP) will be too large relative to the model truth. On the  
459 other hand, a model using the GM-based version of GEOMETRIC as-is with no splitting is expected to largely behave  
460 like a coarse resolution model. We thus expect that the corresponding modelled meridional overturning circulation  
461 will be too weak, because the parameterisation used as-is ends up taking over and removing contributions from explicit  
462 eddies permitted by the model resolution (cf. Fig. 1 of Mak et al., 2023), and the associated modelled heat transport  
463 and NPP is too small. Our hypothesis is that GEOMETRIC with splitting is able to better capture physical and  
464 biogeochemical responses displayed by an eddy-rich model truth, but in a way that is physically consistent. The use  
465 of splitting has been shown to allow the explicit and parameterised eddy components to co-exist (Mak et al., 2023).  
466 The resulting responses are largely like that of an eddy-permitting calculation without parameterisation, but with an  
467 extra contribution affecting the mean state from the parameterisation, so that the modelled stratification, the meridional  
468 overturning circulation, and the magnitude of the modelled heat transports and NPP are closer to the model truth.

469 Table 2 summarises the metrics of interest in this work. The general conclusion is that, indeed, the use of  
470 GEOMETRIC and splitting broadly improves upon the modelled biases relative to the eddy-rich model truth over both  
471 the eddy-permitting models with no parameterisation or with the GM-based version of GEOMETRIC applied as-is,  
472 in the expected way detailed in the previous paragraph, under both the control and idealised climate change scenario.  
473 We reiterate that, while the more detailed analyses performed suggest that the eddy contribution (explicit and/or  
474 parameterised) to tracer transport is rather small, the eddies are essential for shaping the mean-state, which ultimately  
475 leads to substantial changes in the bulk diagnostics (Couespel et al., 2021; Ruan et al., 2023). It should be noted that  
476 the model sensitivities could still be improved upon. While the use of splitting certainly improves upon the use of a  
477 GM-based parameterisation as-is in the eddy-permitting regime (consistent with the results of Mak et al. 2023), there  
478 are cases where the sensitivities of the diagnostics are not necessarily improved by the use of the splitting algorithm,  
479 although there is also no strong evidence that the case with no parameterisation is better either. Nevertheless, the  
480 results are promising, supporting the conclusion that the use of a GM-based scheme in eddy-permitting is possible  
481 and desirable if the splitting procedure is employed. Practically, since the field splitting procedure via the application  
482 of the spatial filter is not performed every time-step (here it is performed every model day, on the assumption that the  
483 large-scale evolves on a slower time-scale), the computational costs are rather minimal, roughly around 5% additional  
484 cost for the present idealised model configuration at the eddy-permitting resolution (cf., Mak et al., 2023).

485 The present results do not invalidate the conclusions drawn in Ruan et al. (2023), which demonstrates that the use  
486 of the GM-based version of GEOMETRIC improves the modelled state and sensitivities as compared to a standard  
487 prescription of the GM-coefficient  $\kappa_{\text{gm}}$  as a constant in a *coarse* resolution model. It is however largely true that the  
488 main factor leading to improvements in the modelled mean states appears to come from a model becoming eddy-



| Diagnostic   | R12 values    | R4 values     | SPLIT values  | GEOM values    | Improve by SPLIT |
|--|---------------|---------------|---------------|----------------|------------------|
| <b>overturning circulation (Sv)</b><br>(Fig. 4a-d and 9a-d)  |               |               |               |                |                  |
| $L^2$ mismatch rel. R12 (CTL)  | —             | 1.21          | 1.09          | 1.98           | ✓                |
| $L^2$ mismatch rel. R12 (CC)   | —             | 0.70          | 0.69          | 1.58           | —                |
| <b>northern mixed layer depth (m)</b><br>(Fig. 4e-h and 9e-h)                                      |               |               |               |                |                  |
| median (CTL)   | 504           | 765           | 664           | 311            | ✓                |
| median (CC)  | 347 (-31.2%)  | 478 (-37.5%)  | 422 (-36.5%)  | 225 (-27.6%)   | ✓ (✓)            |
| quartile range (CTL)   | 232           | 439           | 401           | 197            | ✓                |
| quartile range (CC)  | 111 (-52.4%)  | 199 (-54.6%)  | 172 (-57.1%)  | 128 (-34.8%)   | ✓ (×)            |
| <b>northward heat transport (PW)</b><br>(Fig. 5a)  |               |               |               |                |                  |
| area average (CTL)   | 3.89          | 7.29          | 4.41          | -0.41          | ✓                |
| area average (CC)  | 4.67 (+20.0%) | 5.05 (-30.7%) | 3.17 (-28.2%) | 0.56 (-235.8%) | ✓ (-)            |
| sensitivity ( $L^2$ )  | 2.47          | 3.03          | 2.10          | 1.41           | ✓                |
| <b>vertical heat transport (<math>10^{-3}</math> PW)</b><br>(Fig. 5b)                              |               |               |               |                |                  |
| area average upward (CTL)  | 2.76          | 5.74          | 4.24          | 1.15           | ✓                |
| area average downward (CTL)  | 3.44          | 4.63          | 3.39          | 0.84           | ✓                |
| area average upward (CC)   | 3.41 (+23.4%) | 6.46 (+12.6%) | 5.40 (+27.4%) | 1.07 (-6.9%)   | ✓ (✓)            |
| area average downward (CC)   | 3.18 (-7.5%)  | 4.96 (+7.2%)  | 4.35 (+28.4%) | 1.12 (+26.3%)  | ✓ (-)            |
| sensitivity ( $L^2$ )  | 0.013         | 0.009         | 0.014         | 0.001          | ✓                |
| <b><math>\text{NO}_3^-</math> concentration (<math>\text{mmol N m}^{-3}</math>)</b><br>(not shown) |               |               |               |                |                  |
| area average (CTL)   | 12.02         | 11.49         | 11.81         | 10.55          | ✓                |
| area average (CC)  | 11.05 (-8.1%) | 10.90 (-5.2%) | 11.03 (-6.6%) | 10.17 (-3.6%)  | ✓ (✓)            |
| sensitivity ( $L^2$ )  | 1.00          | 0.65          | 0.86          | 0.64           | ✓                |
| <b>NPP (<math>\text{mmol N m}^{-2} \text{ day}^{-1}</math>)</b><br>(Fig. 6 and 10)                 |               |               |               |                |                  |
| area average (CTL)   | 2.64          | 2.83          | 2.61          | 1.31           | ✓                |
| area average (CC)  | 2.18 (-17.2%) | 2.36 (-16.5%) | 2.18 (-16.6%) | 1.07 (-18.3%)  | ✓ (-)            |

Table 2: Summary of diagnostics and their sensitivities for the set of calculations, all analysed within the analysis domain between  $y = 25$  and  $45^\circ \text{ N}$  ( $S_1$  and  $S_3$  in the text) and  $z = -700 \text{ m}$ , except for mixed layer depth, which is analysed north of  $y = 45^\circ \text{ N}$  in the deep water formation region. The bracketed numbers denote the percentage differences of the relevant diagnostic between the climate change and control scenario.  $L^2$  sensitivity denotes the area-weighted average root-mean-square difference between the climate change and control scenario. A dash is given if there is no obvious evidence that SPLIT leads to an improvement over R4. Note that the values of the northward heat transport here are larger than those reported in Ruan et al. (2023), which was computed from an integral over the whole model depth, and was an inconsistent choice on our part.

489 permitting. Some part of the observed differences with coarse resolution models could be attributed to the presence of  
490 the non-trivial bathymetric slope (sample calculations not shown), but the results seem to suggest that the statement  
491 “a GM-based parameterization turns an eddy-permitting model into an expensive coarse resolution model” that we  
492 hypothesised is overly simplified (e.g., the differences in the prescribed grid-scale viscosity). Using a parameterisation  
493 as-is appears to degrade the representation of the *mean* states. For the present model, it seems to be possible to tune  
494 the parameters accordingly to reproduce a reasonable mean state (e.g., the GEOM calculation but with  $\alpha = 0.025$ ),  
495 but the resulting model has an explicit eddy kinetic energy that is too low (the parameterisation here largely impacts  
496 the Western Boundary Current region; not shown), implying the *variability* has been affected. The splitting approach  
497 appears to be able to retain both of the desirable features of the explicit eddies and some action of the GM-based  
498 schemes in the present work and previous work of Mak et al. (2023), and displays aspects of scale-awareness that  
499 allow the parameterisation to be used across multiple grid resolutions without re-tuning. It is certainly true that the  
500 statistics of the resolved eddies could be different in eddy-permitting regimes relative to eddy-rich/resolving regimes,  
501 and quantifying the difference (as well as providing proposals for any fixes) should be considered in a future work.

502 The present work only investigates the use of splitting with a GM-based scheme, and does not consider more

503 advanced procedures of tapering of  $\kappa_{gm}$  as the shallow ocean is approached (e.g., Wei et al., 2022, 2024; Nummelin and  
504 Isachsen, 2024), although sample experiments with and without any tapering seem to make no significant quantitative  
505 difference to our results (not shown). The present work also does not employ isoneutral mixing (e.g., Redi, 1982;  
506 Griffies, 1998), which is known to modify the tracer transport rates and/or modify the ocean state (e.g., Jones and  
507 Abernathy, 2019; Holmes et al., 2022; Chouksey et al., 2022). One subtlety highlighted in Mak et al. (2023) is  
508 that extra mixing along the *large*-scale stratification profile may lead to significant diapycnal fluxes across the actual  
509 resolve stratification, and it is not clear whether the splitting approach should be used in that context. The proposed  
510 safer option is that diffusion should remain along the *full* modelled isopycnal profile, either by saving extra variables  
511 during model run-time, or recomputing the isopycnal slopes. Sample diagnostics from calculations in the present  
512 model configuration at eddy-permitting resolution but with extra diffusion along the full and large-scale isopycnal  
513 profile are provided in Appendix A. The use of isoneutral diffusion appear to lead to a damping of the explicit eddy  
514 activity, more so when the state-aware GEOMETRIC is employed. There appears to be a positive feedback loop,  
515 where isoneutral diffusion modifies the underlying tracer distribution and thus stratification, leading to changes in  $\kappa_{gm}$   
516 through GEOMETRIC, and modifying the stratification via the resulting eddy-induced velocity. The results presented  
517 in Appendix A further illustrate the complexities of tuning and utilising parameterisations, and question a perceived  
518 view that increasing isoneutral diffusion increases the rate of ventilation but not necessarily the pathways, which is  
519 not true if state-aware GM-based schemes are utilised. A comprehensive exploration associated with the extra degrees  
520 of freedom and possible positive feedback loops from including isoneutral mixing is beyond the scope of the present  
521 paper, but is under investigation and will be reported in a future publication.

522 We have not considered in this work the inclusion of backscatter (e.g., Bachman, 2019; Jansen et al., 2019;  
523 Yankovsky et al., 2023), which could energise the Western Boundary Current, strengthen the too weak overturning  
524 in the subtropical gyre, and/or modify the tracer transport rates to further improve on both the physical and  
525 biogeochemical diagnostics of interest. The use of the splitting algorithm is not mutually exclusive of backscatter, and  
526 we refer the reader to the various subtleties one has to be aware of that has already been discussed in the work of Mak  
527 et al. (2023).

528 Probing and constraining the uncertainties of the splitting approach with GM-based GEOMETRIC scheme and  
529 its impacts on physical and biogeochemical responses is necessary with the increasing prevalence of eddy-permitting  
530 models. The assessments are essential for climate projections in realistic global configurations, initial conditions,  
531 atmospheric forcing, modelled biogeochemical processes, and so forth (e.g., Berthet et al., 2019; Swearer et al.,  
532 2019; Séférian et al., 2019; Couespel et al., 2024). The splitting approach provides one part of a solution to the  
533 problem of representing mesoscale eddy effects in numerical ocean modelling in eddy-permitting regime, and further  
534 investigations into other mesoscale eddy parameterisations are still necessary. An ongoing line of investigation relates  
535 to the use of the splitting procedure with a nonlinear equation of state and with backscatter in a global eddy-permitting  
536 model, and results from the associated research will be reported elsewhere in due course.

537 More generally, this work shows that our procedure of interest leads to an improvement in the modelled  
538 biogeochemical response in a physically consistent and expected way. We advocate that similar assessments for both  
539 the modelled mean state and its sensitivities (to forcing scenarios, free parameters, or otherwise) being performed  
540 in relation to other parameterisation approaches, be they deterministic, stochastic and/or data-driven. As highlighted  
541 in Ruan et al. (2023), a reasonable biogeochemical response could arise from a physically inconsistent response.  
542 Ultimately one should be aiming at procedures that get the ‘right’ answer for the ‘right’ reasons, and such assessments  
543 provide evidence in support of a procedure’s soundness and/or robustness in other regimes.

## 544 Acknowledgments

545 This research was funded by both the RGC General Research Fund 16304021 and the Center for Ocean Research  
546 in Hong Kong and Macau, a joint research center for ocean research between Laoshan Laboratory and Hong Kong  
547 University of Science and Technology. The numerical model modifications, analyses code and sample model data may  
548 be found on Zenodo at <http://dx.doi.org/10.5281/zenodo.11498192>. We thank the two anonymous referees  
549 for their supporting comments that have lead to an improvement in the presentation of the article.

## 550 Appendix A. Inclusion of isoneutral diffusion

551 In this section, we provide sample numerical results for the R4 and SPLIT calculations employing isoneutral  
552 diffusion; analogous results for GEOM have been omitted, since the results are largely similar to that reported in  
553 the Appendix of Ruan et al. (2023). When a harmonic tracer diffusion along a isoneutral direction is switched on,  
554 the biharmonic horizontal tracer diffusion is switched off; the harmonic operator is expected to largely supersede  
555 the action of the biharmonic operator since it damps over a broader length-scale (cf. in Fourier space, these would  
556 correspond to a damping of  $-k^2$  and  $-k^4$  where  $k$  is a representative wavenumber). A diffusivity of  $\kappa_{\text{iso}} = 500 \text{ m}^2 \text{ s}^{-1}$  is  
557 utilised which, while possibly on the slightly large side, demonstrates on why the use of isoneutral diffusion together  
558 with a state-aware GM-based parameterisation requires more care than is perhaps acknowledged in the literature.

559 As noted in Mak et al. (2023), diffusing along the isoneutral direction associated with the large-scale isopycnals  
560 might lead to uncontrolled diapycnal fluxes, and a safer option is to diffuse along the isoneutral direction associated  
561 with the *full* isopycnals. For completeness, however, we tried both approaches, with experiments termed R4(Redi\_full)  
562 and SPLIT(Redi\_full), which employs isoneutral diffusion along the full isopycnals, and SPLIT(Redi\_large), which  
563 has isoneutral diffusion along the large-scale isopycnals computed from the splitting algorithm. To get a sense of the  
564 immediate impacts of employing isoneutral diffusion, we show in Fig. A.12a, b, d, e, g the surface relative vorticity  
565 for the relevant calculations without and with isoneutral diffusion. The presence of isoneutral diffusion in the R4  
566 cases (panels a and d) leads to some damping of the explicit fluctuations (although possibly not to the same extent  
567 as that reported in Mak et al. 2023; see their Fig. 2b). The damping might be expected, since isoneutral diffusion  
568 would erode tracer gradients, which by geostrophic balance would have an impact on the flow field of the baroclinic  
569 eddies, such as that seen in the relative vorticity field. A more dramatic damping is seen when GEOM is utilised,  
570 regardless of whether isoneutral diffusion is along the full isopycnals (panel e) or the large-scale isopycnals (panel g),  
571 relative to the case with no isopycnal diffusion (panel b). SPLIT(Redi\_full) appears to experience the largest damping,  
572 some of which can presumably be attributed to the eddy-induced velocity via increases in the resulting  $\kappa_{\text{gm}}$  (panel f).  
573 There is still noticeable damping in SPLIT(Redi\_large) (panel g) even if the changes in  $\kappa_{\text{gm}}$  are rather mild (panel h),  
574 providing extra evidence that the isoneutral diffusion has an effect on the explicit variability. The associated damping  
575 can also be seen in the time-averaged sense by measures of the domain-integrated explicit eddy kinetic energy for  
576 example (not shown): the decrease in domain-integrated eddy kinetic energy is found to be of a larger percentage in  
577 the corresponding SPLIT experiments compared to the corresponding R4 experiments.

578 This increase in  $\kappa_{\text{gm}}$  we argue to result from isoneutral diffusion modifying the tracer distribution and the  
579 stratification, leading to changes in  $\kappa_{\text{gm}}$  via the GEOMETRIC parameterisation (through both the prescription of  $\kappa_{\text{gm}}$   
580 in Eq. 5 and via the eddy energy budget in Eq. 6), which further leads to changes in the stratification and modifying  
581  $\kappa_{\text{gm}}$ . Such a positive feedback loop is absent in cases where there is no GM-based parameterisation employed (as in  
582 R4 here), or in cases where  $\kappa_{\text{gm}}$  is fixed (as seen in Appendix of Ruan et al. 2023); the splitting approach reduces the  
583 degree of but does not remove this positive feedback loop.

584 Table A.3 shows the relevant metrics diagnosed from the R4 and SPLIT calculations with isoneutral diffusion  
585 active, to be compared with the corresponding values in Table 2. As a summary, it may be seen that the R4 calculation  
586 with isoneutral diffusion remain very similar to that without, with relatively minor *increases* in the relevant transports  
587 (meridional and vertical heat transports, increased nitrate concentration), resulting in marginally larger NPP values.  
588 The same cannot be said of the SPLIT calculation with isoneutral diffusion. SPLIT(Redi\_full) experiences large  
589 shoaling of the mixed layer depths (the median decreases by about 200 meters in the control case, and about 100  
590 meters in the climate change case), and a significant decrease in both the meridional and vertical heat transports, which  
591 are symptoms of a substantially reduced meridional overturning circulation consistent via changes in the stratification  
592 from increases in the value of  $\kappa_{\text{gm}}$  (cf. observations in Ruan et al. 2023). Curiously, the resulting nitrate concentration  
593 increases somewhat. However, the corresponding NPP value noticeably decreases, and the decrease in NPP with  
594 increasing  $\kappa_{\text{gm}}$  is consistent with the results from Ruan et al. (2023). On the other hand, the metrics associated with  
595 SPLIT(Redi\_large) are not entirely unlike that of R4(Redi\_full), with an overly deep mixed layer, rather large transport,  
596 and a rather large NPP. This could have arisen from the additional transport due to the isoneutral diffusion, but also  
597 possibly from the expected spurious diapycnal mixing arising from the isoneutral diffusion but along the direction of  
598 the large-scale rather than full isopycnals. The latter is somewhat harder to quantify and is beyond the scope of the  
599 present work, although there are frameworks for doing so (e.g., Lee et al., 2002; Megann, 2018).

600 The results here highlight further complexities in utilising isoneutral diffusion and eddy-induced advection

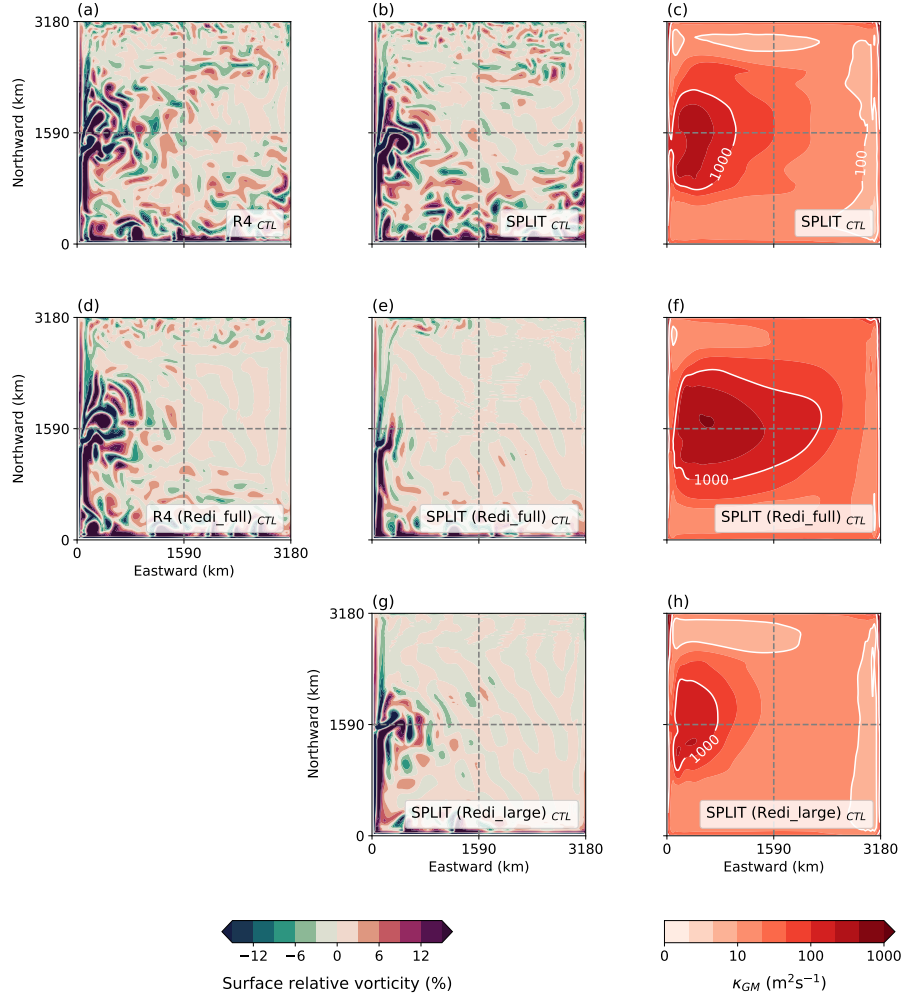


Figure A.12: Snapshots of the surface relative vorticity (in units of the planetary vorticity  $f_0$ ) for (a, d) the R4 cases, and (b, e, g) the SPLIT cases, without isoneutral diffusion, with isoneutral diffusion along the full isopycnal slopes, and with isoneutral along the large-scale isopycnal slopes. We show in (c, f, h) the corresponding  $\kappa_{gm}(x, y, t)$  values (in units of  $\text{m}^2\text{s}^{-1}$ ) for the SPLIT cases. Where isoneutral diffusion is active, the value of the diffusivity is  $\kappa_{gm} = 500 \text{ m}^2 \text{ s}^{-1}$ .

| Diagnostic  | R4(Redi_full) values | SPLIT(Redi_full) values | SPLIT(Redi_large) values |
|---|----------------------|-------------------------|--------------------------|
| <b>overturning circulation (Sv)</b>   |                      |                         |                          |
| $L^2$ mismatch rel. R12 (CTL)   | 1.25                 | 1.36                    | 1.71                     |
| $L^2$ mismatch rel. R12 (CC)  | 0.65                 | 1.08                    | 0.98                     |
| <b>northern mixed layer depth (m)</b>   |                      |                         |                          |
| median (CTL)  | 773                  | 479                     | 930                      |
| median (CC)   | 461 (-40.4%)         | 292 (-39.0%)            | 494 (-46.9%)             |
| quartile range (CTL)  | 492                  | 332                     | 551                      |
| quartile range (CC)   | 211 (-57.0%)         | 174 (-47.6%)            | 239 (-56.6%)             |
| <b>northward heat transport (PW)</b>  |                      |                         |                          |
| area average (CTL)  | 7.49                 | 1.08                    | 6.57                     |
| area average (CC)   | 5.20 (-30.6%)        | 1.63 (+50.9%)           | 3.54 (-46.1%)            |
| sensitivity ( $L^2$ )   | 2.97                 | 1.66                    | 3.57                     |
| <b>vertical heat transport (<math>10^{-3}</math> PW)</b>                            |                      |                         |                          |
| area average upward (CTL)   | 6.03                 | 1.86                    | 4.36                     |
| area average downward (CTL)   | 4.80                 | 1.54                    | 2.62                     |
| area average upward (CC)  | 6.17 (+2.3%)         | 1.49 (-20.1%)           | 5.59 (+28.2%)            |
| area average downward (CC)  | 5.05 (+5.2%)         | 1.38 (-10.4%)           | 4.28 (+63.1%)            |
| sensitivity ( $L^2$ )   | 0.006                | 0.003                   | 0.006                    |
| <b><math>\text{NO}_3^-</math> concentration (<math>\text{mmol N m}^{-3}</math>)</b> |                      |                         |                          |
| area average (CTL)  | 11.61                | 12.56                   | 11.82                    |
| area average (CC)   | 11.01 (-5.1%)        | 11.76 (-6.4%)           | 11.30 (-4.4%)            |
| sensitivity ( $L^2$ )   | 0.65                 | 1.03                    | 0.58                     |
| <b>NPP (<math>\text{mmol N m}^{-2} \text{ day}^{-1}</math>)</b>                     |                      |                         |                          |
| area average (CTL)  | 2.88                 | 2.13                    | 2.89                     |
| area average (CC)   | 2.42 (-15.9%)        | 1.62 (-23.9%)           | 2.50 (-13.6%)            |

Table A.3: Summary of diagnostics and their sensitivities for calculation with isoneutral diffusion active in R4, and active on the full-scale in SPLIT, and active on the large-scale in the SPLIT with codes modified ( $\kappa_{\text{iso}} = 500 \text{ m}^2 \text{ s}^{-1}$  in all of these calculations), to be compared to values in Table 2. All metrics were diagnosed within the analysis domain between  $y = 25$  and  $45^\circ \text{ N}$  ( $S_1$  and  $S_3$  in the text) and  $z = -700 \text{ m}$ , except for mixed layer depth, which is analysed north of  $y = 45^\circ \text{ N}$  in the deep water formation region. The bracketed numbers denote the percentage differences of the relevant diagnostic between the climate change and control scenario.  $L^2$  sensitivity denotes the area-weighted average root-mean-square difference between the climate change and control scenario.

601 parameterisations together, particularly when state-aware parameterisations are used, because of possible feedback  
602 loops with the increased complexity of the parameterisations. In the present model, inclusion of isoneutral diffusion  
603 has rather weak effect on the R4 calculations, and there appears to be a positive feedback loop present when a state-  
604 aware parameterisation for the eddy-induced advection such as GEOMETRIC is utilised. Further work is still needed  
605 on methodologies for tuning strategies for the parameterisations, or possibly on a parameterisation that unifies the  
606 two separate but dynamically related processes, which are really manifestations of the same underlying baroclinic  
607 turbulence.

## 608 References

- 609 Bachman, S. D., 2019. The GM+E closure: A framework for coupling backscatter with the Gent and McWilliams parameterization. *Ocean Modell.*  
610 136, 85–106.
- 611 Beech, N., Rackow, T., Semmler, T., Danilov, S., Wang, Q., Jung, T., 2022. Long-term evolution of ocean eddy activity in a warming world. *Nature*  
612 *climate change* 12 (10), 910–917.
- 613 Berthet, S., S  ferian, R., Bricaud, C., Chevallier, M., Voltaire, A., Eth  , C., 2019. Evaluation of an online grid-coarsening algorithm in a global  
614 eddy-admitting ocean biogeochemical model. *J. Adv. Model. Earth Syst.* 11, 1–25.
- 615 Chang, C., Adcroft, A., Zanna, L., Hallberg, R., Griffies, S. M., 2023. Remote versus local impacts of energy backscatter on the North Atlantic  
616 SST biases in a global ocean model. *Geophys. Res. Lett.* 50, e2023GL105757.
- 617 Charney, J. G., 1971. Geostrophic turbulence. *J. Atmos. Sci.* 28, 1087–1095.
- 618 Chelton, D. B., Schlax, M. G., Samelson, R. M., 2011. Global observations of nonlinear mesoscale eddies. *Prog. Oceanog.* 91, 167–216.

619 Chouksey, A., Grisel, A., Chouksey, M., Eden, C., 2022. Changes in global ocean circulation due to isopycnal diffusion. *J. Phys. Oceanogr.* 52,  
620 2219–2235.

621 Couespel, D., Lévy, M., Bopp, L., 2021. Oceanic primary production decline halved in eddy-resolving simulations of global warming.  
622 *Biogeosciences* 18, 4321–4349.

623 Couespel, D., Lévy, M., Bopp, L., 2024. Stronger oceanic CO<sub>2</sub> sink in eddy-resolving simulations of global warming. *Geophys. Res. Lett.* 51,  
624 e2023GL106172.

625 Eden, C., Greatbatch, R. J., 2008. Towards a mesoscale eddy closure. *Ocean Modell.* 20, 223–239.

626 Fox-Kemper, B., Adcroft, A. J., Böning, C. W., Chassignet, E. P., Curchitser, E. N., Danabasoglu, G., Eden, C., England, M. H., Gerdes, R.,  
627 Greatbatch, R. J., Griffies, S. M., Hallberg, R. W., Hanert, E., Heimbach, P., Hewitt, H. T., Hill, C. N., Komuro, Y., Legg, S., Le Sommer, J.,  
628 Masina, S., Marsland, S. J., Penny, S. G., Qiao, F., Ringler, T. D., Treguier, A. M., Tsujino, H., Uotila, P., Yeager, S. G., 2019. Challenges and  
629 prospects in ocean circulation models. *Front. Mar. Sci.* 6, 65.

630 Gaspar, P., Grégoris, Y., Lefevre, J., 1990. A simple eddy kinetic energy model for simulations of the oceanic vertical mixing: Tests at station papa  
631 and long-term upper ocean study site. *J. Geophys. Res.* 95, 16179–16193.

632 Gent, P. R., McWilliams, J. C., 1990. Isopycnal mixing in ocean circulation models. *J. Phys. Oceanogr.* 20, 150–155.

633 Gent, P. R., Willebrand, J., McDougall, T. J., McWilliams, J. C., 1995. Parameterizing eddy-induced tracer transports in ocean circulation models.  
634 *J. Phys. Oceanogr.* 25, 463–474.

635 Griffies, S. M., 1998. The Gent–McWilliams skew flux. *J. Phys. Oceanogr.* 28, 831–841.

636 Griffies, S. M., Winton, M., Anderson, W. G., Benson, R., Delworth, T. L., Dufour, C. O., Dunne, J. P., Goddard, P., Morrison, A. K., Rosati, A.,  
637 Wittenberg, A. T., Yin, J., Zhang, R., 2015. Impacts on ocean heat from transient mesoscale eddies in a hierarchy of climate models. *J. Climate*  
638 28 (3), 952–977.

639 Grooms, I., 2015. A computational study of turbulent kinetic energy transport in barotropic turbulence on the *f*-plane. *Phys. Fluids* 27, 101701.

640 Hallberg, R., 2013. Using a resolution function to regulate parameterizations of oceanic mesoscale eddy effects. *Ocean Modell.* 72, 92–103.

641 Hewitt, H. T., Fox-Kemper, B., Pearson, B., Roberts, M., Klocke, D., 2022. The small scales of the ocean may hold the key to surprises. *Nat. Clim.*  
642 *Change* 12, 496–499.

643 Hewitt, H. T., Roberts, M., Mathiot, P., Biastoch, A., Blockley, E., Chassignet, E. P., Fox-Kemper, B., Hyder, P., Marshall, D. P., Popova, E.,  
644 Treguier, A., Zanna, L., Yool, A., Yu, Y., Beadling, R., Bell, M. J., Kuhlbrodt, T., Arsouze, T., Bellucci, A., Castruccio, F., Gan, B., Putrasahan,  
645 D., Roberts, C. D., Van Roekel, L., Zhang, Q., 2020. Resolving and parameterising the ocean mesoscale in earth system models. *Curr. Clim.*  
646 *Change Rep.* 6, 137–152.

647 Hoegh-Guldberg, O. R., Cai, R., Poloczanska, E. S., Brewer, P. G., Sundby, S., Hilmi, K., Fabry, V. J., Jung, S., 2014. The ocean. In: Barros, V. R.,  
648 Field, C. B., Dokken, D. J., Mastrandrea, M. D., Mach, K. J., Bilir, T. E., Chatterjee, M., Ebi, K. L., Estrada, Y. O., Genova, R. C., Girma, B.,  
649 Kissel, E. S., Levy, A. N., MacCracken, S., Mastrandrea, P. R., White, L. (Eds.), *Climate Change 2014: Impacts, Adaptation, and Vulnerability.*  
650 *Part B: Regional Aspects. Contribution of Working Group II to the Fifth Assessment Report of the Intergovernmental Panel on Climate Change.*  
651 Cambridge University Press, pp. 1655–1731.

652 Holmes, R. M., Groeskamp, S., Stewart, K., McDougall, T. J., 2022. Sensitivity of a coarse-resolution global ocean model to spatially variable  
653 neutral diffusion. *J. Adv. Model. Earth Syst.* 14, e2021MS002914.

654 Jackson, L., Hughes, C. W., Williams, R. G., 2006. Topographic control of basin and channel flows: the role of the bottom pressure torques and  
655 friction. *J. Phys. Oceanogr.* 36, 1786–1805.

656 Jansen, M. F., Adcroft, A., Khani, S., Kong, H., 2019. Toward an energetically consistent, resolution aware parameterization of ocean mesoscale  
657 eddies. *J. Adv. Model. Earth Syst.* 1, 1–17.

658 Jansen, M. F., Adcroft, A. J., Hallberg, R., Held, I. M., 2015a. Parameterization of eddy fluxes based on a mesoscale energy budget. *Ocean Modell.*  
659 92, 28–41.

660 Jansen, M. F., Held, I. M., Adcroft, A. J., Hallberg, R., 2015b. Energy budget-based backscatter in an eddy permitting primitive equation model.  
661 *Ocean Modell.* 92, 15–26.

662 Jones, C. S., Abernathy, R. P., 2019. Isopycnal mixing controls deep ocean ventilation. *Geophys. Res. Lett.* 46, 13144–13151.

663 Juricke, S., Danilov, S., Koldunov, N., Oliver, M., Sein, D. V., Sidorenko, D., Wang, Q., 2020. A kinematic kinetic energy backscatter  
664 parametrization: From implementation to global ocean Simulations. *J. Adv. Model. Earth Syst.* 12 (12), e2020MS002175.

665 Klocker, A., Marshall, D. P., 2014. Advection of baroclinic eddies by depth mean flow. *Geophys. Res. Lett.* 41, L060001.

666 LaCasce, J. H., Brink, K. H., 2000. Geostrophic turbulence over a slope. *J. Phys. Oceanogr.* 30 (6), 1305–1324.

667 Lee, M.-M., Coward, A. C., Nurser, A. G., 2002. Spurious diapycnal mixing of deep waters in an eddy-permitting global ocean model. *J. Phys.*  
668 *Oceanogr.* 32, 1522–1535.

669 Lévy, M., Iovino, D., Resplandy, L., Klein, P., Madec, G., Tréguier, A., Masson, S., Takahashi, K., 2012. Large-scale impacts of submesoscale  
670 dynamics on phytoplankton: Local and remote effects. *Ocean Modell.* 43–44, 77–93.

671 Lévy, M., Klein, P., Tréguier, A., Iovino, D., Madec, G., Masson, S., Takahashi, K., 2010. Modifications of gyre circulation by sub-mesoscale  
672 physics. *Ocean Modell.* 34, 1–15.

673 Lindgren, F., Rue, H., Lindström, J., 2018. An explicit link between Gaussian fields and Gaussian Markov random fields: The stochastic partial  
674 differential equation approach. *J. R. Stat. Soc. Series B Stat. Methodol.* 73, 423–498.

675 Madec, G., 2008. NEMO ocean engine. Note du Pôle de modélisation, Institut Pierre-Simon Laplace (IPSL), No. 27.

676 Mak, J., Avdis, A., David, T. W., Lee, H. S., Na, Y., Yan, F. E., 2022a. On constraining the mesoscale eddy energy dissipation time-scale. *J. Adv.*  
677 *Model. Earth Syst.* 14, e2022MS003223.

678 Mak, J., Maddison, J. R., Marshall, D. P., Munday, D. R., 2018. Implementation of a geometrically informed and energetically constrained  
679 mesoscale eddy parameterization in an ocean circulation model. *J. Phys. Oceanogr.* 48, 2363–2382.

680 Mak, J., Maddison, J. R., Marshall, D. P., Ruan, X., Wang, Y., 2023. Scale-awareness in an eddy energy constrained mesoscale eddy  
681 parameterization. *J. Adv. Model. Earth Syst.* 15, e2023MS003886.

682 Mak, J., Marshall, D. P., Madec, G., Maddison, J. R., 2022b. Acute sensitivity of global ocean circulation and heat content to eddy energy dissipation  
683 time-scale. *Geophys. Res. Lett.* 49, e2021GL097259.

684 Marshall, D. P., Maddison, J. R., Berloff, P. S., 2012. A framework for parameterizing eddy potential vorticity fluxes. *J. Phys. Oceanogr.* 42,  
685 539–557.

686 Megann, A., 2018. Estimating the numerical diapycnal mixing in an eddy-permitting ocean model. *Ocean. Modell.* 121, 19–33.

687 Ni, Q., Zhai, X., Wang, G., Hughes, C. W., 2020a. Widespread mesoscale dipoles in the global ocean. *J. Geophys. Res. Oceans* 125,  
688 e2020JC016479.

689 Ni, Q., Zhai, X., Wang, G., Marshall, D. P., 2020b. Random movement of mesoscale eddies in the global ocean. *J. Phys. Oceanogr.* 50, 2341–2357.

690 Nummelin, A., Isachsen, P. E., 2024. Parameterizing mesoscale eddy buoyancy transport over sloping topography. *ESS Open Archive*.

691 Perezhogin, P., Zanna, L., Fernandez-Granda, C., 2023. Generative data-driven approaches for stochastic subgrid parameterizations in an idealized  
692 ocean model. *J. Adv. Model. Earth Syst.* 15, e2023MS003681.

693 Pradal, M., Gnanadesikan, A., 2014. How does the Redi parameter for mesoscale mixing impact global climate in an Earth system model? *J. Adv.*  
694 *Model. Earth Syst.* 6, 586–601.

695 Redi, M. H., 1982. Oceanic isopycnal mixing by coordinate rotation. *J. Phys. Oceanogr.* 12, 1154–1158.

696 Roberts, M. J., Jackson, L. C., Roberts, C. D., Meccia, V., Docquier, D., Koenigk, T., Ortega, P., Moreno-Chamarro, E., Bellucci, A., Coward, A. C.,  
697 Drijfhout, S., Exarchou, E., Gutjahr, O., Hewitt, H., Iovino, D., Lohmann, K., Putrasahan, D., Schiemann, R., Seddon, J., Terray, L., Xu, X.,  
698 Zhang, Q., Chang, P., Yeager, S. G., Castruccio, F. S., Zhang, S., Wu, L., 2020. Sensitivity of the Atlantic Meridional Overturning Circulation  
699 to model resolution in CMIP6 HighResMIP simulations and implications for future changes. *J. Adv. Model. Earth Syst.* 12, e2019MS002014.

700 Ruan, X., Couespel, D., Lévy, M., Mak, J., Wang, Y., 2023. Assessing the impact of ocean mesoscale eddy parameterizations on physical and  
701 biogeochemical responses: Diffusive closures in non-eddy ocean models. *Ocean Modell.* 183, 102204.

702 Sférian, R., Nabat, P., Michou, M., Saint-Martin, D., Voldoire, A., Colin, J., Decharme, B., Delire, C., Berthet, S., Chevallier, M., Sénési, S.,  
703 Franchisteguy, L., Vial, J., Mallet, M., Joetzjer, E., Geoffroy, O., Guérémy, J., Moine, M., Msadek, R., Ribes, A., Rocher, M., Roehrig, R.,  
704 Salas-y-Méllia, D., Sanchez, E., Terray, L., Valcke, S., Waldman, R., Aumont, O., Bopp, L., Deshayes, J., Éthé, C., Madec, G., 2019. Evaluation  
705 of CNRM Earth System Model, CNRM-ESM2-1: Role of Earth system processes in present-day and future climate. *J. Adv. Model. Earth. Syst.*  
706 11 (12), 4182–4227.

707 Smith, R. D., Gent, P. R., 2004. Anisotropic Gent–McWilliams parameterization for ocean models. *J. Phys. Oceanogr.* 34, 2541–2564.

708 Stewart, A. L., Thompson, A. F., 2013. Connecting Antarctic cross-slope exchange with Southern Ocean overturning. *J. Phys. Oceanogr.* 43 (7),  
709 1453–1471.

710 Swearer, S. E., Tremblé, E. A., Shima, J. S., 2019. A review of biophysical models of marine larval dispersal. *CRC Press*.

711 Tokarska, K. B., Stolpe, M. B., Sippel, S., Fischer, E. M., Smith, C. J., Lehner, F., Knutti, R., 2020. Past warming trend constrains future warming  
712 in CMIP6 models. *Sci. Adv.* 6, eaaz9549.

713 Torres, R., Waldman, R., Mak, J., Sférian, R., 2023. Global estimation of the eddy kinetic energy dissipation from a diagnostic energy balance.  
714 *Geophys. Res. Lett.* 50, 2023GL104688.

715 Wang, Y., Stewart, A. L., 2018. Eddy dynamics over continental slopes under retrograde winds: Insights from a model inter-comparison. *Ocean*  
716 *Modell.* 121, 1–18.

717 Waterman, S., Hoskins, B. J., 2013. Eddy shape, orientation, propagation, and mean flow feedback in western boundary current jets. *J. Phys.*  
718 *Oceanogr.* 43, 1666–1690.

719 Waterman, S., Jayne, S. R., 2012. Eddy-driven recirculations from a localized transient forcing. *J. Phys. Oceanogr.* 42, 430–447.

720 Wei, H., Wang, Y., Mak, J., 2024. Parameterizing eddy buoyancy fluxes across prograde shelf/slope fronts using a slope-aware GEOMETRIC  
721 closure. *J. Phys. Oceanogr.* 54, 359–377.

722 Wei, H., Wang, Y., Stewart, A. L., Mak, J., 2022. Scalings for eddy buoyancy fluxes across prograde shelf/slope fronts. *J. Adv. Model. Earth. Syst.*  
723 14, e2022MS003229.

724 Whittle, P., 1963. Stochastic processes in several dimensions. *Bull. Int. Stat. Inst.* 40, 974–994.

725 Wilder, T., Munday, X. Z. D. R., Joshi, M., 2023. Constraining an eddy energy dissipation rate due to relative wind stress for use in energy  
726 budget-based eddy parameterisations. *Ocean Sci.* 19, 1669–1686.

727 Yankovsky, E., Bachman, S. D., Smith, K. S., Zanna, L., 2023. Vertical structure and energetic constraints for a backscatter parameterization of  
728 ocean mesoscale eddies. *ESS Open Archive*.